# Four-wave mixing microscopy of nanostructures

Yong Wang, Chia-Yu Lin, Alexei Nikolaenko, Varun Raghunathan, and Eric O. Potma*

Department of Chemistry & Beckman Laser Institute, University of California, Irvine, Irvine, California 92697, USA

*Corresponding author: epotma@uci.edu

Received May 6, 2010; revised July 14, 2010; accepted July 27, 2010; published September 10, 2010 (Doc. ID 128079)

The basics of four-wave mixing (FWM) and recent advances in FWM microscopy are reviewed with a particular emphasis on applications in the field of nanomaterials. The vast progress in nanostructure synthesis has triggered a need for advanced analytical tools suitable to interrogate nanostructures one at a time. The single-nanostructure sensitivity of optical microscopy has solidified the optical approach as a reliable technique for examining the electronic structure of materials at the nanoscale. By zooming in on the individual, optical microscopy has permitted detailed investigations of the linear optical response of nanomaterials such as semiconducting quantum dots and plasmon active nanometals. Besides studying the linear optical properties of nanostructures, optical microscopy has also been used to probe the nonlinear optical properties of nanoscale materials. FWM microscopy, a coherent third-order optical imaging technique, has shown great potential as a tool for investigating the nonlinear optical response of nanostructures. FWM microscopy not only permits the characterization of the nonlinear susceptibility of individual nanostructures, it also offers a route to explore the time-resolved dynamics of electronic and vibrational excitations on single structures. In addition, FWM produces strong signals from nanomaterials that are compatible with fast imaging applications, which holds promise for biological imaging studies based on nanoparticle labels that are not prone to photobleaching. 

OCIS codes: 190.4380, 180.4315, 160.4236.

# Four-wave mixing microscopy of nanostructures

Yong Wang, Chia-Yu Lin, Alexei Nikolaenko, Varun Raghunathan, and Eric O. Potma

## 1. Introduction

Over the past decade the field of material sciences has witnessed an enormous surge in the fabrication of materials on the submicrometer and nanometer scale ($1\ \mu\text{m} - 1$ nm). It has been recognized that materials, including metals, semiconducting materials, inorganic materials, organic and composite materials, on such small length scales often exhibit properties that are markedly different from bulk materials. Approaching length scales well below the size of optical wavelengths, the optical properties are particularly sensitive to the downsizing of materials. Examples include the strong optical response of semiconducting quantum dots (QDs) [1] and enhanced optical effects at metal particles due to surface plasmon resonances [2].

Along with the advances in nanostructured material synthesis there is a growing need for characterizing the optical properties of these novel materials. Optical spectroscopy of ensemble samples of nanostructured materials often provides a great amount of information on the nature of the excitations that govern the optical properties of the material. Nonetheless, ensembles of nanostructured materials generally display a large amount of heterogeneity in terms of size and shape of the structures. Because the ensemble contains a distribution of such properties, bulk optical spectroscopy measurements may not suffice in providing a detailed picture of the optical response at the single particle level. In this regard, optical microscopy of individual particles and structures has proved to be an invaluable complement to ensemble optical spectroscopy measurements.

The resolution of the optical microscope is typically limited by diffraction of light, rendering the spatial resolution in the range of $0.5 - 0.2\ \mu$m. This resolution is insufficient for resolving the spatial features of most nanostructured materials. Nonetheless, optical microscopy is the method of choice for characterizing the optical properties of isolated structures that are spatially separated from neighboring structures by more than the distance specified by the Rayleigh criterion [3]. In cases where better resolving power is needed, superresolution approaches and near-field optical methods can be used to improve the resolution down to the tens of nanometers range [4–6].

Linear optical microscopy has been used extensively to examine nanostructures on a particle-by-particle basis. For instance, near-field optical microscopy measurements have been used to characterize the surface plasmon resonances on individual gold nanoparticles [7,8]. Similarly, far field microscopy has been employed to study the extinction of single metal particles and structures [9,10], and the time-dependent fluorescence properties (blinking) of semiconducting QDs

[11,12]. Such measurements provide close-ups of the properties of individual particles, information that is skewed in ensemble measurements.

In addition to examining the linear optical properties of nanostructured materials, the optical microscope also provides a platform for investigating the nonlinear optical properties of individual structures. The enhanced linear optical response of nanostructures is often accompanied by an enhancement of the nonlinear optical properties as well. The high optical nonlinearity of materials at the nanoscale has many interesting potential applications, as such materials can serve as efficient optical frequency converters and as nonlinear optical labels for biological imaging. Research in this direction has reported efficient second- and third-harmonic generation (THG) of light at metallic nanostructures [13–15], two-photon excited emission from inorganic nanoparticles [16,17], and frequency mixing at semiconducting QDs [18]. Beyond characterization of the static nonlinear optical response of nanomaterials, the nonlinear optical microscope also offers the opportunity to explore the time-resolved optical response of individual structures on ultrafast time scales.

In this review we will discuss the application of a nonlinear optical microscopy technique, called four-wave mixing (FWM) microscopy, for the purpose of visualizing and characterizing nanostructured materials. FWM microscopy is a third-order nonlinear technique sensitive to the third-order susceptibility $\chi^{(3)}$ of the nanomaterial. The technique is based on three incident laser fields with frequencies $\omega_1$, $\omega_2$, and $\omega_3$, which interact through the material's $\chi^{(3)}$ to generate a signal field at frequency $\omega_4$. The colors of the incident light can be chosen such that the emitted light is spectrally separated from the incoming radiation, which facilitates detection of the signal in an optical microscope. The FWM signal is, in principle, sensitive to both the electronic as well as the vibrational properties of the material. A coherent spectroscopic technique, FWM microscopy also offers the possibility of probing the ultrafast evolution and the dephasing dynamics of the optical excitation in nanomaterials. In the bulk spectroscopy configuration, the FWM technique has been widely used for interrogating the ultrafast excitation dynamics of ensemble nanostructured materials. When applied to microscopy, such information can be attained while maintaining the submicrometer spatial resolution of far-field microscopy, and along with it the possibility of examining the ultrafast dynamics of individual nanoparticles.

As a general microscopy implementation, FWM imaging has naturally evolved from the coherent anti-Stokes Raman scattering (CARS) imaging technique [19,20]. In CARS, the incoming frequencies $\omega_1$ and $\omega_3$ are typically identical, while $\omega_2$ is frequency shifted by a characteristic Raman frequency $\Delta$ of the material ($\omega_2 = \omega_1 - \Delta$). The CARS signal emitted at $\omega_4 = 2\omega_1 - \omega_2$ is enhanced by the vibrational resonance $\Delta$ and forms an excellent probe for molecules with strong Raman vibrational modes [21]. The CARS technique is the most common application of FWM microscopy, particularly in the field of biological and biomedical imaging [22–24]. Other examples of Raman sensitive FWM microscopy techniques are stimulated Raman scattering (SRS) [25,26] and optical Kerr effect microscopy [27]. In all these vibrational FWM implementations, the incoming and detected frequencies are chosen such as to optimize the sensitivity of the experiment to the vibrational properties of the sample.

While the vibrational sensitivity of FWM microscopy stems from Raman resonances, the technique is by no means limited to the measurement of vibrational modes. By tuning the incoming or emitted frequencies into an electronic reso-

nance of the material, selected electronic excitations can be probed. In addition, electronically resonant excitation of the material is accompanied by an enhanced FWM response. The electronically enhanced FWM signal facilitates detection of an otherwise weak nonlinear response. This is particularly relevant to the study of nanostructured materials, where the amount of material is often so small that limited FWM may be expected under electronically nonresonant conditions.

In the following sections, we will discuss the principles of FWM microscopy and its application to the study of nanostructured materials. We will put particular emphasis on the electronic enhancement of the FWM response and how this effect can be used to visualize and characterize nanomaterials, including metals, inorganic nanoparticles, and molecular nanostructures.

## 2. Four-Wave Mixing

### 2.1. Third-Order Susceptibility

FWM is a category of light–matter interactions in which three incoming waves, indicated here as $\omega_1$, $\omega_2$ and $\omega_3$, in the material generate a fourth wave of frequency $\omega_4$. Assuming that the three incident waves have frequencies in the visible or near-infrared range, the incoming electric fields $\boldsymbol{E}(\omega_i)$ (with $i=1,2,3$) interact with the material's electrons to induce a nonlinear polarization $\boldsymbol{P}^{(3)}(\omega_4)$ in the illuminated volume. The magnitude of the polarization is determined by the strength of the incident fields and the efficiency with which the material can be polarized. The latter is indicated with the third-order nonlinear susceptibility $\chi^{(3)}$, a measure of the material's response to the incoming fields. The components of the induced polarization at a particular location $\boldsymbol{r}$ in the sample can be written as

$$P_i^{(3)}(\omega_4=\omega_1+\omega_2+\omega_3;\boldsymbol{r})=\epsilon_0\chi_{ijkl}^{(3)}(-\omega_4;\omega_1,\omega_2,\omega_3;\boldsymbol{r})E_j(\omega_1,\boldsymbol{r})E_k(\omega_2,\boldsymbol{r})E_l(\omega_3,\boldsymbol{r}), \tag{1}$$

where $\epsilon_0$ is the vacuum permittivity and $\chi_{ijkl}^{(3)}$ are the components of a fourth-rank tensor. The indices $(i,j,k,l=1,2,3)$ refer to the Cartesian polarization directions of the emitted and incoming fields. The first frequency between parentheses in the notation $\chi_{ijkl}^{(3)}(-\omega_4;\omega_1,\omega_2,\omega_3)$ corresponds to the emitted field, and the following frequencies refer to the incident fields in no particular time order. The sign of each frequency can be either positive or negative. An interpretation of the sign associated with the field is found in quantized field theory, where a negative frequency corresponds to an emitted field and a positive frequency to a field absorbed by the material.

The magnitude of the third-order susceptibility, and thus the FWM signal, strongly depends on the incident and induced frequencies. In general, $\chi^{(3)}$ is high whenever single or combination frequencies are in resonance with eigenfrequencies of the material. Therefore, to quantitatively model the third-order susceptibility, the quantum mechanical eigenstates of the material have to be taken into account explicitly. Understanding the resonances contained in the expression for $\chi^{(3)}$ is key for relating the detected FWM signals to the electronic and vibrational properties of the material.

As shown by Pershan and co-workers, the third-order nonlinear susceptibility in the weak field limit is best modeled through a perturbation expansion of the system's wave function (or density function) to the third-order in the incoming fields [28]. Because of the permutation arrangements of the electric field frequencies $\omega_i$ and the number of relevant quantum states in the material, the number of terms that contributes to the third-order susceptibility can be very large. For instance, assuming four relevant quantum states of the material indicated in Fig. 1(a), the number of terms for each output frequency combination ($\omega_4=\omega_1+\omega_2+\omega_3$) is 384 [29]. Under the assumption that initially just the ground state is populated, and grouping together the terms with indistinguishable structures, the number of terms for each output frequency reduces to 24 [30,31].

To explore the resonances contained in $\chi^{(3)}$ we write the third-order susceptibility of a single output frequency $\omega_4$ in terms of groups with different two-photon resonances [30]:

$$\begin{aligned}\chi^{(3)}_{ijkl}(-\omega_4;\omega_1,\omega_2,\omega_3) = {} & \frac{g_{il}(\omega_4,\omega_3)f_{jk}(\omega_1,\omega_2)}{\omega_{ba}-(\omega_1+\omega_2)-i\Gamma_{ba}} + \frac{f^*_{jk}(-\omega_1,-\omega_2)g^*_{il}(-\omega_4,-\omega_3)}{\omega_{ba}+(\omega_1+\omega_2)+i\Gamma_{ba}} \\ & + \frac{g_{ik}(\omega_4,\omega_2)f_{jl}(\omega_1,\omega_3)}{\omega_{ba}-(\omega_1+\omega_3)-i\Gamma_{ba}} + \frac{f^*_{jl}(-\omega_1,-\omega_3)g^*_{ik}(-\omega_4,-\omega_2)}{\omega_{ba}+(\omega_1+\omega_3)+i\Gamma_{ba}} \\ & + \frac{g_{ij}(\omega_4,\omega_1)f_{kl}(\omega_2,\omega_3)}{\omega_{ba}-(\omega_2+\omega_3)-i\Gamma_{ba}} + \frac{f^*_{kl}(-\omega_2,-\omega_3)g^*_{ij}(-\omega_4,-\omega_1)}{\omega_{ba}+(\omega_2+\omega_3)+i\Gamma_{ba}}\end{aligned} \tag{2}$$

where the factors containing the one-photon resonances are defined as

$$g_{xy}(\omega_i,\omega_j) = \left(\frac{N}{\hbar^3}\right)^{1/2}\sum_n\left(\frac{\mu^x_{an}\mu^y_{nb}}{\omega_{na}-\omega_i-i\Gamma_{na}} + \frac{\mu^x_{an}\mu^y_{nb}}{\omega_{na}+\omega_j+i\Gamma_{nb}}\right),$$

$$f_{xy}(\omega_i,\omega_j) = \left(\frac{N}{\hbar^3}\right)^{1/2}\sum_n\left(\frac{\mu^x_{bm}\mu^y_{na}}{\omega_{na}-\omega_i-i\Gamma_{na}} + \frac{\mu^x_{bm}\mu^y_{na}}{\omega_{na}-\omega_j-i\Gamma_{na}}\right). \tag{3}$$

Here $N$ is the density of the material considered, $\mu^x_{ij}$ is the $x$ component of the transition dipole between states $(i,j)$, and the $\Gamma$ factors are related to the spectral width of the resonances. Substituting Eqs. (3) into Eq. (2) leads to a total of 24 different terms that contribute to the signal at frequency $\omega_4$.

The frequencies can be chosen to be either positive or negative. To simplify the discussion, we shall consider here the single degenerate case of output frequency $\omega_4=2\omega_1-\omega_2$. We will also assume that $\omega_1>\omega_2$. This particular choice of frequencies includes the CARS type of interaction, which was first demonstrated by Maker and Terhune in 1965 [21]. Other common FWM frequency combinations are schematically given in Fig. 1. To examine the resonances contained in $\chi^{(3)}(-\omega_4;\omega_1,\omega_1,-\omega_2)$ we will first assume that all incoming and induced frequencies are much smaller than any electronic resonance frequencies of the material, i.e., that the material is transparent with respect to the frequencies considered.

### 2.1a. Transparent Materials: Two-Photon Resonances

In the absence of one-photon resonances, the $g(\omega_i,\omega_j)$ and $f(\omega_i,\omega_j)$ factors are real and relatively small. In this case, the dominant contributions to

Figure 1

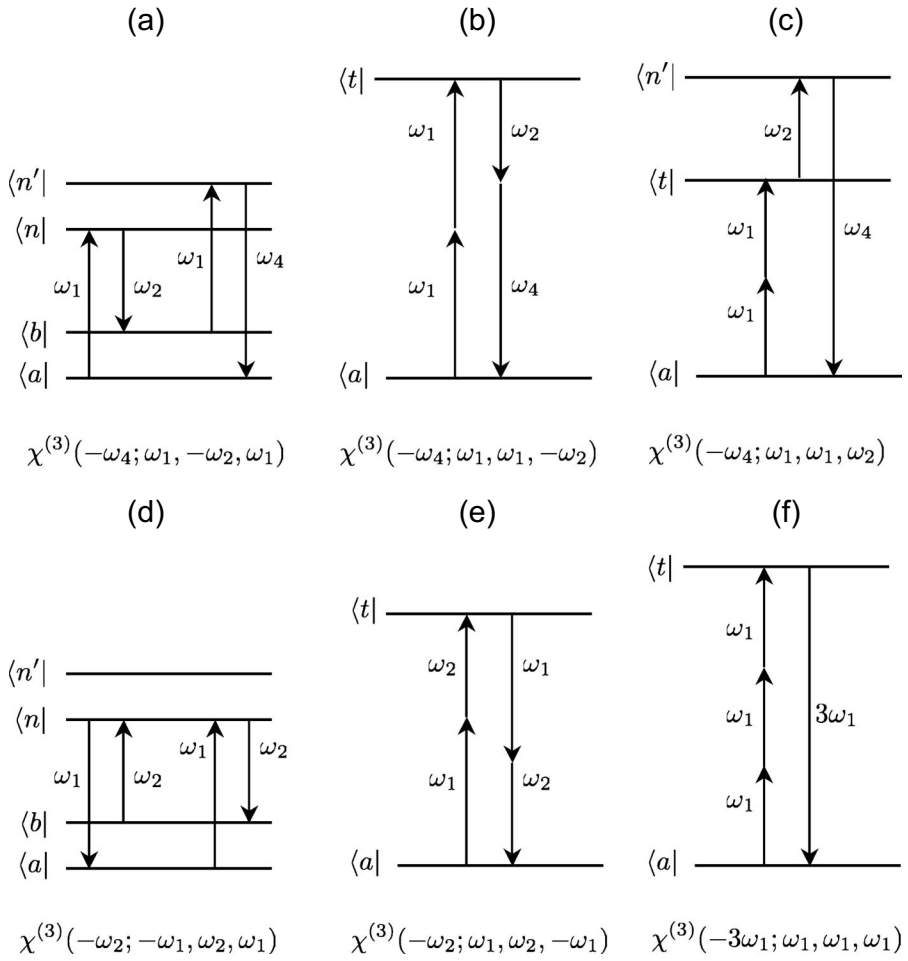


Energy diagrams of several representative FWM processes. In these diagrams, $\langle a|$ is the ground state, $\langle b|$ and $\langle t|$ are intermediate states, and $\langle n|$, $\langle n'|$ are higher-energy states in the material. Note that all of these states, except for the ground state, can represent either eigenstates of the material or virtual states. (a) CARS excitation scheme. If $\langle b|$ is a vibrational state, then this scheme corresponds to vibrational CARS. (b) TPA-enhanced difference-frequency mixing, an electronically resonant scheme. This scheme has also been referred to as stimulated parametric emission (SPE). The $\langle t|$ level corresponds to a two-photon accessible eigenstate of the material. (c) TPA-enhanced sum-frequency mixing. (d) SRS excitation scheme. If $\langle b|$ is a vibrational state, then this scheme corresponds to vibrational SRS. The emitted field is at the same frequency as one of the incident beams ($\omega_2$). (e) TPA-enhanced difference-frequency mixing. Like SRS, this scheme results in emission at $\omega_2$. (f) THG. The $\langle t|$ level corresponds to a one- or three-photon accessible eigenstate of the material.

$\chi^{(3)}(-\omega_4;\omega_1,\omega_1,-\omega_2)$ are the terms with two photon resonances. Two types of two-photon resonances may occur. The first type of resonance occurs when the frequency combination $\omega_1+\omega_1$ approaches an electronic eigenfrequency $\omega_t$ of the material. This type of resonance is usually referred to as the two-photon absorption (TPA) contribution to the third-order susceptibility [30,32]. A second two-photon resonance is found when the difference frequency $\omega_1-\omega_2$ corre-

sponds to a material eigenfrequency $\omega_r$. The latter process is a Raman-type resonance. When all incident fields are in the visible or near-infrared range, the Raman resonances typically correspond to vibrational resonances of molecules or to phonon modes of solid state materials. Note, however, that in materials with electronic band structures, Raman-type resonances may occur that are purely electronic. Based on the above assumptions, the nonlinear susceptibility in scalar form at the output frequency $\omega_4 = 2\omega_1 - \omega_2$ can be summarized as [32]

$$\chi^{(3)}(-\omega_4;\omega_1,\omega_1,-\omega_2) = \chi^{(3)}_{NR} + \sum_t \left[ \frac{A_t}{\omega_t - 2\omega_1 - i\Gamma_t} + \frac{A_t}{\omega_t + 2\omega_1 + i\Gamma_t} \right] + \sum_r \frac{A_r}{\omega_r - (\omega_1 - \omega_2) - i\Gamma_r}, \tag{4}$$

where the amplitudes $A_t$ and $A_r$ are proportional to $|g(\omega_i,\omega_j)|^2$, a frequency-independent function when none of the incident and induced frequencies are close to a one-photon resonance of the material. The first term on the right-hand side of Eq. (4) contains all the contributions to $\chi^{(3)}(-\omega_4;\omega_1,\omega_1,-\omega_2)$ that do not contain a two-photon resonance. This nonresonant contribution is real and relatively small, but it is generally not negligible. It corresponds to the intrinsic electronic polarizability of the material when driven at the incident frequencies, which is nonzero even in the absence of any nearby material resonances.

The second term on the right-hand side contains the TPA-enhanced resonances. The summation is over all the two-photon accessible states $|t\rangle$ of the material. This part of the nonlinear susceptibility closely resembles the two-photon scattering susceptibility $\chi^{(3)}(-\omega_1;\omega_1,\omega_1,-\omega_1)$, the imaginary part of which can be related to the TPA cross section [30,33]. Consequently, the two-photon absorptivity can be directly assessed with two-photon resonant $\chi^{(3)}$ measurements. This method has been used extensively to determine TPA cross sections of various materials [34,35]. The TPA enhancement of $\chi^{(3)}$ can also be used as a contrast mechanism in FWM microscopy. Imaging contrast is derived from chromophores with high TPA cross sections at the $2\omega_1$ frequency. The TPA-enhanced FWM imaging method has recently been applied to visualize dye-stained polymer beads [36,37] and red blood cells based on the two-photon resonances of hemoglobin [38,39].

The third term on the right-hand side of Eq. (4) is the Raman resonant contribution to the nonlinear susceptibility. The summation runs over all the Raman allowed states $|r\rangle$ of the material. For the frequency combination chosen here ($\omega_1 > \omega_2$), this term represent the CARS response of the material. Away from two-photon electronic resonances, the Raman term can dominate the nonlinear response of the material. The Raman resonant FWM contribution is most commonly used to examine materials based on their Raman active vibrational modes [21,29,40]. The imaginary part of the Raman resonant contribution is directly related to the cross section for spontaneous Raman scattering [30,41]. Relative to spontaneous Raman scattering, the Raman resonant FWM signal is coherent and can be particularly strong whenever the number of Raman scatterers in the probing volume is high ($N > 10^5$) [42,43]. The higher signal yield makes the CARS approach to vibrational microscopy very attractive, as it permits shorter pixel integration times and fast imaging of microstructured samples [44,45]. In this review, we will call the excitation scheme indicated by the diagram of Fig. 1(a) the CARS excitation process, irrespective of whether the nature of the two-photon Raman process is electronic or vibrational.

### 2.1b. Direct Electronic Excitations: One-Photon Resonances

Close to one-photon resonances of the material, the $g(\omega_i, \omega_j)$ and $f(\omega_i, \omega_j)$ factors are complex and can be of substantial magnitude [31]. The third-order nonlinear susceptibility can now be written as a sum of three major contributions:

$$\chi^{(3)}(-\omega_4;\omega_1,\omega_1,-\omega_2) = \chi^{(3)}_{NR} + \chi^{(3)}_{E}(-\omega_4;\omega_1,\omega_1,-\omega_2) + \chi^{(3)}_{R}(-\omega_4;\omega_1,\omega_1,-\omega_2) \tag{5}$$

The first term on the right-hand side includes all the nonresonant contributions to the nonlinear susceptibility. All one-photon electronically resonant terms are included in $\chi^{(3)}_E$, and the terms that contain a Raman resonance in addition to one-photon resonances are included in $\chi^{(3)}_R$. The Raman resonant terms are of the following form [31]:

$$\chi^{(3)}_R = \frac{N}{\hbar^3}\sum_{n,n'} \frac{\mu_{an}\mu_{nb}\mu_{bn'}\mu_{n'a}}{(\omega_{na}-\omega_4-i\Gamma_{na})(\omega_{ba}-(\omega_1-\omega_2)-i\Gamma_{ba})(\omega_{n'a}-\omega_1-i\Gamma_{n'a})}. \tag{6}$$

The term given in Eq. (6) is significant when $\omega_1$ and $\omega_4$ are close to a one-photon electronic resonance of the material, in addition to a Raman resonance at $\omega_1 - \omega_2$. In case state $b$ is initially populated, extra terms exist with electronic resonances at $\omega_2$ (instead of $\omega_1$) as well. The terms contained in $\chi^{(3)}_E$ are of similar form but lack the intermediate two-photon resonance. The spectral dispersion of the one-photon resonances in $\chi^{(3)}_E$ can be grouped into a complex function $A_E \exp[i\theta_E]$, where $A_E$ is defined as the frequency dependent electronic amplitude and $\theta_E$ is the corresponding electronic phase. A similarly compressed function can also be defined for the one-photon resonances in $\chi^{(3)}_R$, with amplitude $A^r_E$ and phase $\theta^r_E$, which is associated with the Raman mode $r$ at frequency $\omega_{ba}$. Using this notation, the nonlinear susceptibility can be written as [46,47]

$$\chi^{(3)}(-\omega_4;\omega_1,\omega_1,-\omega_2) = \chi^{(3)}_{NR} + A_E\exp[i\theta_E] + \sum_r \frac{A^r_E \exp[i\theta^r_E]}{\omega_r - (\omega_1-\omega_2) - i\Gamma_r}. \tag{7}$$

Compared with the Raman resonant term relevant to transparent materials [Eq. (4)], the Raman resonant component in Eq. (7) can be substantially larger owing to one-photon resonance enhancement. This term is responsible for the high sensitivity of electronically resonant CARS (RCARS), which allows vibrational spectroscopic interrogations of chromophore solutions with concentrations in the micromolar range [48,49].

## 2.2. Magnitude of $\chi^{(3)}$ and Feasibility of Four-Wave Mixing Microscopy

To visualize individual nanostructures in a nonlinear FWM microscope, the third-order interaction between the incident light and the material needs to be sufficiently strong to produce detectable signals. Compared with samples probed in conventional bulk FWM spectroscopy, generating detectable third-order signals from nanostructures is particularly challenging because the amount of material probed is smaller by many orders of magnitude. In addition, rapid imaging requires short pixel integration times, typically of the order of mi-

croseconds. These conditions put tight restrictions on both the sensitivity of the FWM microscope and the kind of materials that can be visualized in the nonlinear microscope.

The magnitude of $\chi^{(3)}$ of a given material can be determined in a variety of ways. For nontransparent materials, degenerate FWM (DFWM)[50,51] and reflective-based THG [52,53] have been used. For transparent materials, CARS-based schemes [54], the THG fringe [55,56] and ratio [57,58] method, and the Z-scan technique are commonly applied [59]. Note that these measurements usually refer to the $\chi^{(3)}_{1111}$ component of the third-order nonlinear susceptibility. Depending on the symmetry properties of the material, other components of $\chi^{(3)}$ can have values that are significantly different from the $\chi^{(3)}_{1111}$ component. For more information on how the tensor elements of $\chi^{(3)}$ can be used to examine the structural and orientational properties of the material, the reader is referred to [60,61].

Limiting our discussion to materials illuminated with ultrafast radiation, the third-order nonlinear susceptibility of electronically nonresonant materials in the condensed phase results from the anharmonic motion of electrons and can be estimated to be in the $10^{-14}$ esu range [62]. Measurements on nonresonant transparent materials indeed indicate third-order susceptibilities of such magnitude [55,63]. For instance, the magnitude of $\chi^{(3)}$ of water is $1.3\times10^{-14}$ esu at 1064 nm, which is comparable with the $\chi^{(3)}$ of silica ($1.4\times10^{-14}$ esu) and borosilicate glass ($2.1\times10^{-14}$ esu) [64]. The magnitudes of $\chi^{(3)}$ of some typical materials encountered in biological FWM microscopy are listed in Table 1. Seeing single nanostructured objects with such nonlinear susceptibilities is extremely challenging and is generally below the detection limit of a fast scanning FWM microscope. High-sensitivity FWM imaging of nanostructures is best achieved when the intrinsic nonlinear response of the material is significantly higher. Material properties and mechanisms that improve the detection of nanostructured materials in the FWM microscope include the following:

(1) A high intrinsic $\chi^{(3)}$ of the material. Several materials, including inorganic and semiconducting materials, exhibit third-order susceptibilities that are orders of magnitude higher than the $\chi^{(3)}$ of organic solvents and biological materials.

(2) Electronic enhancement of $\chi^{(3)}$. As discussed above, one- and two-photon electronic resonances can significantly enhance the third-order optical response of the material.

(3) Nanoscale quantum confinement effects. Several materials have been pre-

**Table 1. Third-Order Susceptibility of Several Common Materials and Organic Liquids[a]**

| Material | λ (nm) | $\chi^{(3)}$ (esu) | $n_0$ (3$\omega$) | Ref. |
|---|---|---|---|---|
| Water | 1064 | $1.3\times10^{-14}$ | 1.35 | [64] |
| Glycine (1M aqueous) | 1064 | $1.2\times10^{-14}$ | 1.35 | [64] |
| Vegetable oil | 1064 | $1.9\times10^{-14}$ | 1.47 (590 nm) | [64] |
| Silica | 1064 | $1.4\times10^{-14}$ | 1.48 | [65] |
| BK7 | 1064 | $2.1\times10^{-14}$ | 1.54 | [65] |
| Ethanol | 1064 | $1.7\times10^{-14}$ | 1.38 | [64] |
| $CS_2$ | 1910 | $2.0\times10^{-13}$ | 1.63 | [66] |

[a]The magnitude of $\chi^{(3)}$ was determined from THG measurements. The wavelength of excitation (λ) and the linear refractive index ($n_0$) are given as well.

dicted to exhibit enhanced optical nonlinearities due to the confinement of delocalized electrons in the nanostructure.

(4) Surface plasmon effects. The collective motion of surface electrons in several submicrometer and nanoscopic metallic structures produces a local enhancement of the electric field, which in turn enhances the nonlinear response of the metallic structure.

In the remainder of this paper, we will discuss the third-order nonlinear response from nanostructured materials for the purpose of nonlinear imaging. For a detailed account on the physical origins of the optical nonlinearities in solid state materials, which falls outside the scope of this work, the reader is referred to [67].

## 2.3. Third-Order Nonlinear Emission in the Tight Focusing Limit

In nonlinear optical microscopy, the incident fields are spatially confined to a tight focal spot. The size of the focal volume is determined by the diffraction of light and is typically smaller than 1 $\mu m^3$ for high-numerical-aperture lenses when using visible or near-infrared radiation. The confined probing volume is the primary attribute of the optical microscope, as it allows the examination of individual objects that are spatially separated from their neighbors on the micrometer scale. Moreover, the submicrometer probing volume also reduces background contributions from the surrounding medium, yielding a sensitivity to submicrometer-sized structures that is superior to bulk optical probing methods.

A good description of the amplitude and phase of the focal fields can be obtained from diffraction theory as developed by Richards and Wolf [68]. Assuming no index mismatch and incident light that is $x$ polarized, the focal field can be written in the form shown by Novotny and Hecht as [69]

$$E(\rho,z) = E_0 e^{-ikf} \begin{pmatrix} I_{00} + I_{02}\cos 2\phi \\ I_{02}\sin 2\phi \\ -2iI_{01}\cos\phi \end{pmatrix}. \tag{8}$$

Here, $E_0$ is the field amplitude, $k$ is the wave vector, $f$ is the focal length of the lens, $\phi$ corresponds to the azimuthal angle, and $\rho=(x^2+y^2)^{1/2}$. The quantities $I_{mn}$, with $m=0,1$ and $n=0,\ldots,4$, are one-dimensional integrals with respect to the polar angle $\theta$ and are written as

$$I_{mn}(\rho,z) = \int_0^{\theta'_{\max}} f_w(\theta)\sqrt{\cos\theta}\, g_{mn}(\theta) J_l(k\rho\sin\theta) e^{ikz\cos\theta}\sin\theta d\theta, \tag{9}$$

where $l=n$ if $n\leq m$, and $l=n-m$ if $n>m$. The acceptance angle of the objective is indicated by $\theta'_{\max}$. The function $f_w(\theta)$ is the apodization function [69], which describes the degree of the filling of the back aperture of the objective. Its value is 1 when the back aperture is uniformly filled. The functions $g_{nm}$ are given by $g_{0n}=1+\cos\theta$, $\sin\theta$, $1-\cos\theta$ for $n=0,1,2$ and $g_{1n}=\sin^2\theta$, $\sin\theta(1+3\cos\theta)$, $\sin\theta(1-\cos\theta)$, $\sin^2\theta$, $\sin(1-\cos\theta)$ for $n=0,1,2,3,4$, respectively.

A cross-sectional view ($xy$) of the focal field amplitude of a focused 800 nm laser beam is depicted in Fig. 2(a). The phase of the focal field along the optical axis is shown in Fig. 2(b). The linear phase due to propagation has been subtracted for clar-

Figure 2

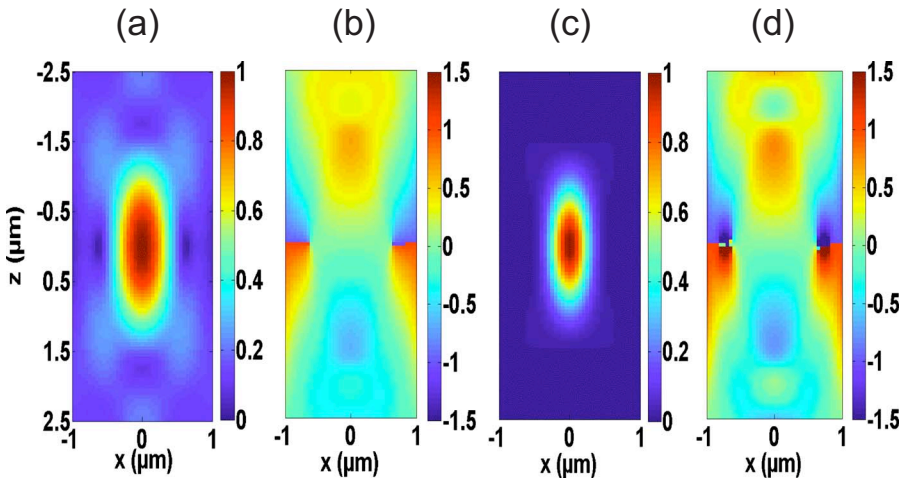


Focal fields of a high-numerical-aperture lens (NA 1.1, water immersion). (a) Focal field amplitude of a 800 nm laser beam. (b) Phase profile of the focal field given in (a). The propagation phase has been subtracted for clarity. (c) Amplitude of the CARS excitation field $E_1^2E_2^*$ with $\lambda_1=800$ nm and $\lambda_2=1064$ nm. (d) Phase profile of the excitation field given in (c).

ity. It is evident that the phase before the focal plane and the phase after the focal plane ($z=0$) are not the same. Along the optical axis, the phase undergoes a full $\pi$-phase swing. This phase swing is known as the Gouy phase shift [70,71].

In Fig. 2(c), the FWM excitation field amplitude is plotted for a CARS-type interaction $\omega_4=2\omega_1-\omega_2$, which is of the form $E_1^2E_2^*$. For this particular excitation profile, the lateral full width at half-maximum of the excitation amplitude is 0.45 $\mu$m, and the axial width is 1.4 $\mu$m. The longitudinal extent of the excitation volume is of the order of an optical wavelength, which implies that phase mismatch between the incident waves and the emitted wave is minimal within the interaction volume. Consequently, phase mismatching effects due to material dispersion, which can be prominent in interaction volumes associated with low numerical aperture lenses, are not a major factor in the signal generation process when high-numerical-aperture lenses are used [72–74].

The phase profile is given in Fig. 2(d). Similar to the phase distribution of a focused laser beam, the spatial phase of the excitation field undergoes an $\sim\pi$ phase shift. This implies that the nonlinear polarization within the focal volume exhibits a focal phase shift roughly similar to that of a forward propagating beam. Consequently, the FWM radiation of the $\omega_4=2\omega_1-\omega_2$ process is not particularly affected by a Gouy phase mismatch. A Gouy phase mismatch is, however, rather prominent for other FWM processes, such as THG, which has a profound effect on the spatial distribution of the emitted third-order signal [75,76].

At locations where the material overlaps with the excitation volume $E_1^2(\mathbf{r})E_2^*(\mathbf{r})$, a nonlinear polarization is induced in the material according to Eq. (1). The induced nonlinear polarization $\mathbf{P}(\omega_4,\mathbf{r})$ at each point $\mathbf{r}$ in the material forms the source of radiation at frequency $\omega_4$. In the far field, the field amplitude at location $\mathbf{R}$ can be approximated by spatially integrating over the contributions of all dipole emitters in the focal volume $V$:

$$\mathbf{E}(\mathbf{R}) = -\int_V \frac{\exp[ik_4|\mathbf{R}-\mathbf{r}|]}{4\pi|\mathbf{R}-\mathbf{r}|^3}(\mathbf{R}-\mathbf{r}) \times [(\mathbf{R}-\mathbf{r}) \times \mathbf{P_4}(\mathbf{r})]d^3\mathbf{r}. \quad (10)$$

Since there is a coherent relation between the dipole emitters within the focal volume, the emitted waves will interfere. This spatial interference defines the shape of the emission profile, which can vary drastically with the size and shape of the illuminated sample structure. A dramatic consequence of the wave interference is the difference between forward and backward propagating light. For objects with dimensions below $\lambda_4/4$, the forward and backward radiation is of the same order. For larger objects, the waves in the forward direction constructively interfere, producing strong signals, while destructive interference among the backward propagating waves significantly suppresses the signal observed in the epi-direction. Most nanostructures, however, are of the order of $\lambda_4/4$ or smaller, and the signal detected in the backward direction can be significant.

In Fig. 3, the FWM emission profile of a 50 nm cube object is shown. The emission pattern resembles the radiation profile of a Hertzian dipole, and the amount of signal emitted in the forward and backward channels is roughly similar. Nonetheless, for reasons of enhanced collection efficiency and rejection of the incident light, detection of FWM signals emitted by nanostructures in the epi-direction can often be achieved with a higher signal-to-background ratio than in the forward detection scheme.

Figure 3

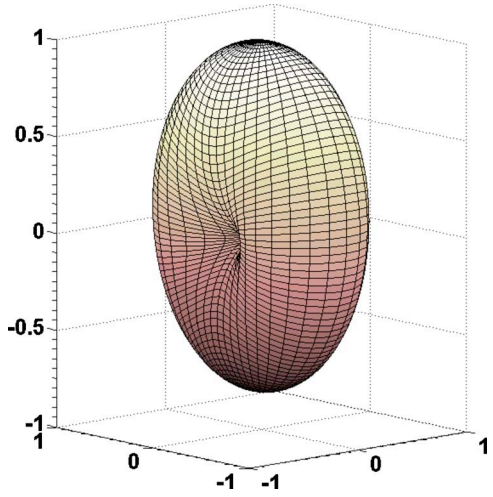


Far-field emission pattern of the FWM CARS response from a 50 nm nanocube in the focus of a NA 1.1 water immersion lens. The CARS excitation volume is given in Figs. 2(c) and 2(d). Note that because of their small size relative to an optical wavelength, the FWM emission from nanoscale objects resembles the emission of a Hertzian dipole, resulting in comparable amounts of radiation in the forward direction and epi-direction.

## 3. Four-Wave Mixing Microscope

The FWM microscope has two main ingredients: an ultrafast laser light source and a scanning optical microscope. For electronically resonant FWM processes, femtosecond lasers are the preferred light sources, as their spectral pulse widths are compatible with the width of the one-photon absorption bands of the material, thus optimizing the efficiency of the FWM process. For THG measurements, a single femtosecond laser is sufficient for examining the third-order nonlinear properties of individual nanostructures. Due to the high detection sensitivity of detectors like photomultiplier tubes in the visible range of the spectrum, the laser wavelength is often chosen such that the third-harmonic radiation is within the visible spectral range. Near-infrared fiber lasers, Cr:forsterite lasers, and Ti:sapphire lasers combined with an optical parametric oscillator are light sources that can be conveniently interfaced with an optical microscope for THG measurements [77–79].

In the THG measurements the pump frequency $\omega_1$ and the signal frequency $3\omega_1$ are well separated. This facilitates signal detection by spectral filtering. The ability to isolate the signal spectrally from the incident light is advantageous in FWM microscopy, as spatial separation of the signal is often impractical when working with high-numerical-aperture lenses. This is one of the main reasons why DFWM experiments, where the incident and induced frequencies are similar, are difficult to implement in a microscope configuration. THG experiments are well suited to interrogate materials that are transparent at the incident frequency. The method is, however, less practical for examining materials that are one-photon resonant with the incident frequency. In such cases, an electronic CARS-type scheme is often preferred. In CARS, the signal frequency is separated from the incident light, yet it is often possible to tune the incident frequencies as well as the signal frequency into electronic resonance with the material. The CARS excitation scheme has been successfully applied to visualize metallic [80–83] and semiconducting nanostructures [18,84] in a fast-scanning microscope configuration.

The CARS excitation scheme necessitates two spectrally separated incident frequencies $\omega_1$ and $\omega_2$. This can be achieved by using two separate pulse trains, which are commonly derived from two synchronized lasers [85] or from a synchronously pumped optical parametric oscillator system [86]. If vibrational information is desired, a dual-color picosecond light source can be used to provide the spectral resolution needed to resolve the two-photon Raman process. Although less efficient than femtosecond excitation, the narrow spectral width provided by picosecond light can be helpful in discriminating the narrowband coherent response from the broad incoherent emission that often accompanies the electronic FWM signal (see Subsection 6.3). An example of a FWM microscope based on a dual-color light source is shown in Fig. 4. Alternatively, a single femtosecond laser light source can be used with sufficient bandwidth to synthesize the desired $\omega_1$ and $\omega_2$ pairs for FWM experiments [87–89].

The key components that make up the microscope include the scanner, the high-numerical-aperture lens, and the detector system. Scanning can be achieved either through scanning the sample or by scanning the laser focus. If fast scanning is required, laser beam scanning is the method of choice. Many commercial confocal microscope systems incorporate a fast laser scanning mechanism that can be readily used for FWM imaging experiments. The high-numerical-aperture

Figure 4

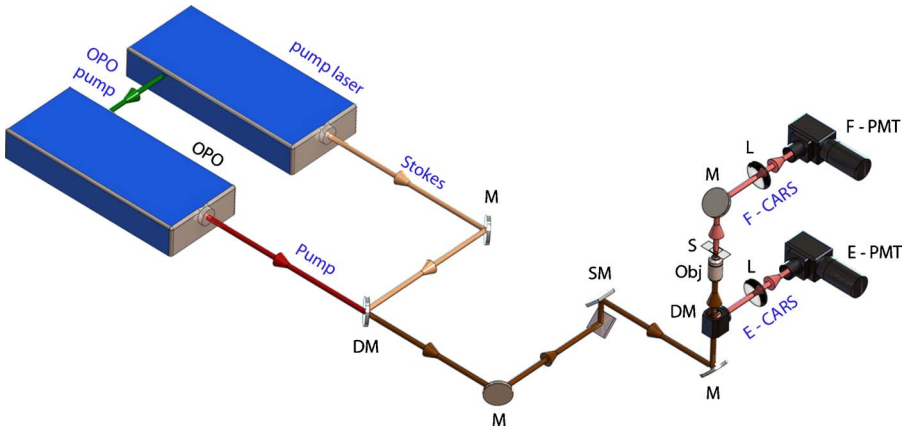


Schematic of a dual-color FWM microscope based on a synchronously pumped optical parametric oscillator (OPO) light source. Two detector channels are used, one in the forward (F) propagating direction and one in the epi-direction (E). M, mirror; DM, dichroic mirror; SM, galvanometric scanning mirrors; Obj, microscope objective lens; S, sample; L, lens; PMT, photomultiplier tube.

lens is the heart and soul of the microscope. The quality of the lens determines the quality of the focal volume. For dual-color FWM experiments, optimal transmission at the incident and emission wavelengths is essential, along with minimum chromatic aberrations of the lens system at the relevant optical wavelengths. For detection of FWM signals that are different from the incident wavelengths, such as CARS and THG signals, detectors with single-photon counting sensitivities are desirable because of the intrinsically low signal yield. A sensitive photomultiplier tube complies with such requirements. Alternative schemes in which the signal field is homodyned with one of the incident fields, as is the case in SRS microscopy [26], or detected through interference with a strong reference beam, as in heterodyne CARS measurements [90], do not require single-photon counting detection sensitivities. These detection schemes benefit from detectors with a large dynamic range and work well with silicon photodiode detectors.

In an inverted optical microscope, the nanostructured sample is typically mounted on a glass or quartz cover slip. The weak signal from nanostructures close to the glass surface can be somewhat enhanced through an interference effect at the cover slip interface. This effect stems from the nonresonant electronic FWM signal generated in the cover slip material. Part of this radiation is back-reflected at the surface, which subsequently interferes with the epi-directed FWM emission from the nanostructure [43]. When the FWM signal from the cover slip is substantially larger than the signal from the nanostructure, this interference effect can boost the signal signatures from the structure of interest, as illustrated in Fig. 5. For nanostructures fabricated on opaque substrates such as silicon wafers, an upright microscope provides the most convenient imaging solution.

Figure 5

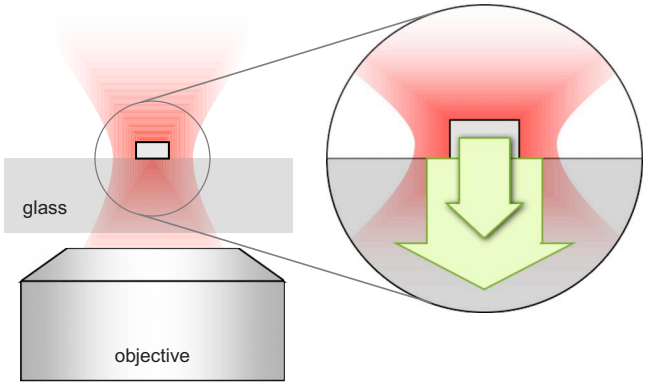


Interference effects in epi-detection of FWM radiation from nanostructures on a glass substrate. The nonresonant FWM in the glass substrate is reflected at the glass/air and glass/nanostructure interface, resulting in a background signal in the epi-channel (large arrow). The FWM field from the nanostructure itself can mix coherently with the background FWM radiation. If the background signal is large, the weak FWM response from nanostructures can be enhanced in a homodyne manner.

## 4. Four-Wave Mixing of Transparent Materials

Far from one or two-photon electronic resonances, the third-order nonlinear response of most materials originates predominantly from nonresonant, anharmonic electron motion and is relatively small [91]. Nonetheless, a significant response can be expected when the volume of the material approaches the FWM excitation volume. Hence, even though the $\chi^{(3)}$ of borosilicate, a common material for microscope cover slips, is of the order of $10^{-14}$ esu, a detectable signal from the glass can be easily observed when the material occupies the entire focal volume. When nanoparticles with high nonlinear susceptibilities are embedded in a glass matrix, the contribution from the glass host cannot always be ignored.

The nonresonant nonlinear response from $SiO_2$ glasses is sufficient for imaging microscopically structured glass objects. In Fig. 6, a 1 $\mu$m silica glass sphere is visualized through two FWM processes, a nonresonant CARS excitation scheme and a dual-color optical Kerr effect excitation scheme [27]. The $\chi^{(3)}$ signals detected through either FWM scheme are strong enough for fast imaging of microstructured glass.

The nonresonant $\chi^{(3)}$ of transparent biological materials and water is similarly in the $10^{-13}$–$10^{-14}$ esu range. The magnitude of the third-order nonlinearity of water in the transparency region is governed mostly by the purely electronic hyperpolarizability, but librational modes and nuclear vibrations may contribute to the nonlinearity when broad bandwidth femtosecond pulses are used [92]. In transparent, heterogeneous biological materials, the nonlinear susceptibility varies both because of intrinsic differences in the electronic hyperpolarizability as well as variable two-photon resonances among the molecular components. The spatially varying nonlinear susceptibility is the source of the vibrationally nonresonant contrast in biological CARS imaging. While often an undesirable signal contribution in vibrational imaging studies, this nonresonant component is nonetheless a material characteristic and

Figure 6

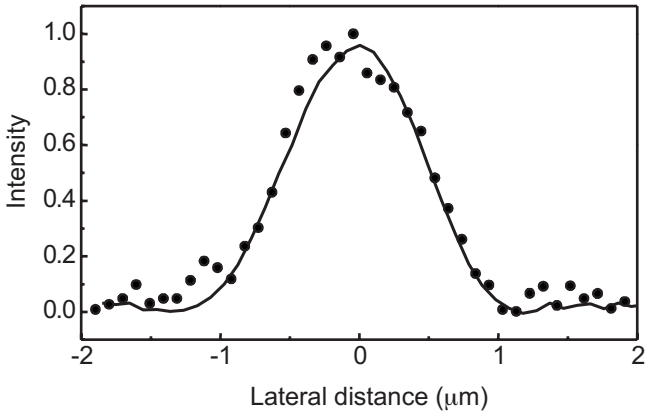


Lateral cross section of a 1 $\mu$m silica bead measured with nonresonant CARS (solid curve) and optical Kerr effect microscopy (dots). Both FWM techniques produce good microscopic contrast from a nonresonant (transparent) material with a low nonlinear susceptibility.

can be used to generate images based on contrast derived from the electronic polarizability [93]. This nonresonant FWM imaging approach has been used to obtain structural and morphological information of biological samples [94].

To a good approximation, the electronic polarizability in aqueous samples is isotropic. In samples that exhibit a degree of spatial organization, however, this assumption is no longer valid. In highly aligned biological materials, such as cellulose and collagen fibers for instance, an orientation dependence of the purely electronic nonlinear susceptibility can be expected. In particular, an anisotropic electronic response is found in materials that exhibit structural order. For example, the directional dependence of $\chi^{(3)}$ has been employed to study the director field orientations in liquid crystals by nonresonant FWM imaging, as illustrated in Fig. 7 [95].

## 5. Four-Wave Mixing Imaging of Semiconducting Nanostructures

The linear optical properties of semiconducting materials are highly dependent on the excitation energy relative to the bandgap energy of the material. Linear excitation with photon energies that exceed the bandgap energy results in the absorption of the photon and the creation of electron and hole charge carriers. Due to Coulombic interactions between the electron and hole, excitonic states are introduced close to the band edge energy. For photon energies $\omega > \omega_{gap}$, the nonlinear response is dominated by the carrier related nonlinearities, which include band filling effects [96–98] and exciton bleaching [99]. Early DFWM studies at photon energies near the bandgap reported high third-order susceptibilities of the order of $10^{-8}$ esu [50,51,100–102]. When excited in the transparency region, no linear excitation of the carriers occurs, and the nonlinear response is governed by the anharmonic motion of the valence electrons. At excitation energies lower than the bandgap energy, away from one-photon resonances, the optical nonlinearity is

Figure 7

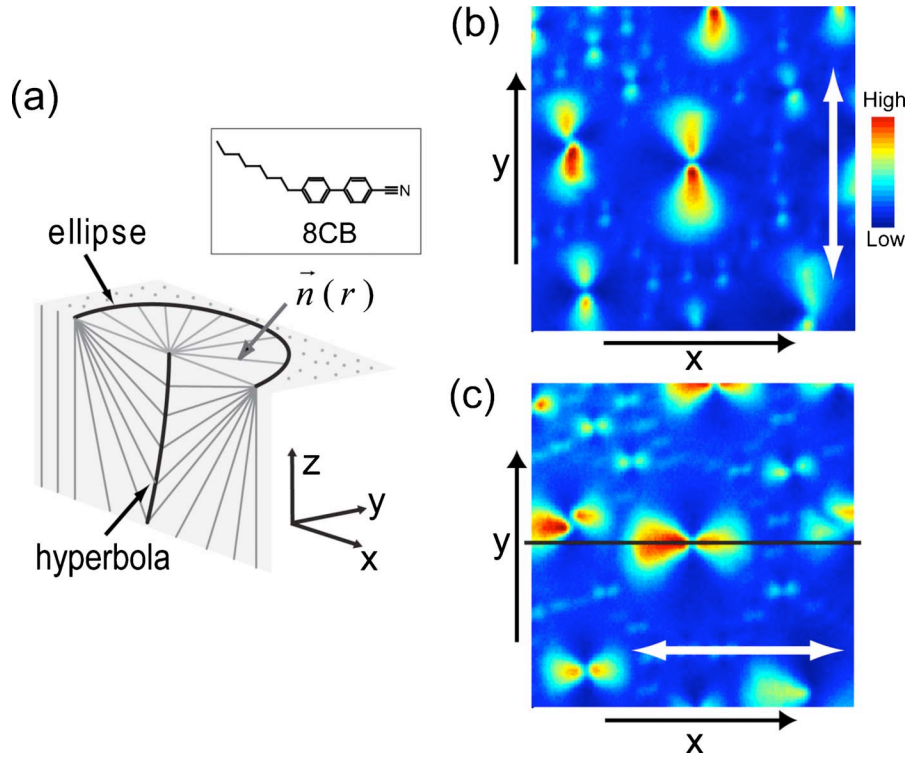


Electronic CARS FWM of liquid crystals. (a) Schematic of the director fields in a smectic A phase of an octylcyano-biphenyl (8CB) liquid crystal. The liquid crystal molecules have a highly anisotropic electronic response, resulting in orientation sensitive FWM images. The conical morphology is known as the focal conic domain (FCD). (b), (c) Horizontally sectioned FWM images of the FCD, indicating highly oriented liquid crystal domains. White arrows represent the laser polarization direction. Reprinted in part with permission from [95]. Copyright 2009, American Institute of Physics.

consequently much weaker. Nonetheless, even in the transparency region, the third-order susceptibility of semiconductor materials is substantially higher than that observed in many other materials. The relatively high magnitudes of $\chi^{(3)}$, in the $10^{-12}$–$10^{-9}$ esu range, render these materials excellent candidates for optical probes in microscopic FWM imaging studies.

Besides the intrinsically high values for $\chi^{(3)}$, several mechanisms may contribute to a further enhancement of the third-order response. In particular, when exciting in the transparency region, multiphoton electronic resonances can boost the optical nonlinearity of the semiconducting material [67,103]. In addition, quantum size effects have been suggested to contribute to an enhanced third-order response as well. Quantum size effects are expected to play a role whenever the dimensions of the material approach the physical size of the exciton wavefunction, which is usually characterized in terms of the exciton Bohr radius [104]. Whereas quantum confinement has a pronounced effect on the linear optical properties of semiconducting materials, it is much less clear how these effects are reflected in the nonlinear response of the material [105].

Below we discuss several semiconductor materials with large optical nonlinearities sufficient to enable detection of FWM signals from single nanoparticles. In each case, we briefly consider the different mechanisms that shape the overall nonlinear response of the nanostructure, and we point toward several applications of such materials in FWM microscopy.

## 5.1. Elemental Semiconducting Materials

Elemental semiconducting materials such as germanium and silicon have third-order nonlinear susceptibilities that are among the highest known for solid state materials. In as early as 1969, Wynne reported CARS-type electronic FWM experiments on various semiconducting bulk materials including germanium and silicon, which revealed $\chi^{(3)}$ magnitudes higher than $10^{-10}$ esu [54]. These measurements were performed at energies much lower than the bandgap, in the transparency region of the materials. Closer to the bandgap of these materials, at energies corresponding to near-infrared wavelengths often used in biological imaging, one- and two-photon resonances raise the magnitude of the third-order susceptibility well into the $10^{-9}$ esu range. These values of $\chi^{(3)}$ are more than four orders of magnitude higher than the third-order susceptibilities of typical biological materials. Given these high optical nonlinearities, it can be expected that nanostructures fabricated from these materials would provide strong FWM probes for imaging purposes. The nonlinear susceptibilities of silicon and germanium are given in Table 2, along with their bandgap energy and linear refractive index.

Many semiconducting materials can be prepared as nanoscopic objects and structures. Silicon nanospheroids, for instance, can be prepared in a variety of ways, such as through laser ablation [108] or through chemical vapor deposition techniques [109], producing silicon particles in the 1–100 nm range. Gold-assisted chemical vapor deposition has been used to grow silicon nanowires in a controlled fashion, producing nanowires with adjustable diameters and lengths [110,111]. The exciton Bohr radius of bulk silicon is 4.9 nm [112], and quantum size effects are expected to become important for nanostructures with radii of the order of a few nanometers. Indeed, strong indications of quantum confinement effects are found in porous silicon, a material that has been shown to contain wirelike crystalline silicon arrays with dimensions in the 2–5 nm range [112]. The band edge in porous silicon is strongly dependent on the size of the nanocrystallites, and a bright luminescence is observed for such materials. The luminescent properties of nanosilicon have already rendered these materials promising candidates for *in vivo* imaging applications [113]. Along with the change in the linear optical response of nanosized silicon, an enhancement of the third-order nonlinear optical properties has been predicted [114]. Evidence for enhancement of $\chi^{(3)}$ in silicon nanomaterials

**Table 2. Third-Order Nonlinear Susceptibility of Elemental Semiconducting Materials[a]**

| Material | λ (nm) | $\chi^{(3)}$ (esu) | $E_g$ (ev) | $\lambda_{edge}$ (nm) | $n_0$ | Ref. |
|---|---|---|---|---|---|---|
| Si | 1064 | $2.5\times10^{-10}$ | 1.11 | 1118 | 3.49 | [53,106] |
| Ge | 1064 | $5.6\times10^{-11}$ | 0.67 | 1853 | 4 | [53,106,107] |

[a]The magnitude of $\chi^{(3)}$ was determined from THG measurements. The wavelength of excitation (λ), the bandgap energy ($E_g$), band-edge absorption wavelength ($\lambda_{edge}$) and the linear refractive index ($n_0$) are given for comparison.

has come from Z-scan measurements on nanoclusters with particle diameters of 1–5 nm. Measurements of the third-order susceptibility of such silicon nanoparticles indicate a modest increase of the magnitude of $\chi^{(3)}$ relative to bulk silicon with decreasing size of the nanocrystallite [109].

FWM experiments on individual silicon nanowires have confirmed the strong nonlinear optical response of silicon nanomaterials. Using polarization dependent FWM microscopy, Jung *et al.* observed a very strong FWM response along the long axis of nanowires prepared through the chemical vapor deposition technique [115]. As shown in Fig. 8(a), the strong FWM signal provides a unique signature of the nanowire, as no spurious multiphoton luminescence from the particles was observed. Unlike the signal from fluorescent probes, the FWM signal from silicon nanowires was not prone to photobleaching, permitting sustained imaging of the nanowire probes in biological samples. The FWM signal from these nanomaterials is brighter than the nonresonant FWM contribution from the biological material itself, which enables identification of silicon nanowire probes in live cells and tissues [115]. In addition, the absence of photobleaching and the high photodamage threshold make silicon nanoparticles ideal candidates for characterizing the imaging properties of the FWM microscope. In Figs. 8(b) and 8(c), the image of a 30 nm silicon nanoparticle is used to examine the size and shape of the focal excitation volume.

Similar to silicon nanostructures, germanium nanoparticles have shown promise as materials with a strong third-order optical response. Compared with silicon, the exciton Bohr radius of germanium is much larger at 24.3 nm [116], which implies that quantum confinement effects can be expected even for larger sized particles. A growing blueshift of the bandgap energy with decreasing size of the germanium nanoparticle has provided proof that the linear optical properties of nanosized germanium are indeed controlled by quantum size effects [117,118]. Similar to silicon, a bright visible photoluminescence is observed for small germanium nanocrystallites, which has been attributed to an alternate lattice structure of germanium atoms in the nanocluster compared with the bulk [119]. Z-scan measurements of germanium nanoclusters performed at excitation energies below the bandgap have shown that $\chi^{(3)}$ is of the order of $10^{-9}$ esu and have indicated that two-photon resonances are important when exciting below the bandgap [117,118].

The strong nonlinear response of silicon and germanium nanoparticles classifies these materials as a promising family of FWM probes. The small size ($>10$ nm) of such particles makes them highly compatible for biological labeling applications. In addition, the toxicity of elemental semiconductor materials is expected to be reduced compared with several metal nanoprobes. Recent progress in the synthesis of elemental semiconductor nanomaterials, including the fabrication of tin colloids [120] and tellurium nanorods [121], is likely to expand the list of FWM active nanoprobes.

## 5.2. Metal Oxide Nanoparticles

Compared with elemental semiconductor materials, the third-order susceptibility in metal oxides is substantially lower, of the order of $10^{-11}$–$10^{-12}$ esu [122,123]. Values of several metal oxide materials are listed in Table 3. Despite the somewhat weaker optical nonlinearities, metal oxide nanoparticles are attractive candidates for FWM imaging applications because of relatively simple preparation methods and their commercial availability. The bandgap of most metal oxides, in-

Figure 8

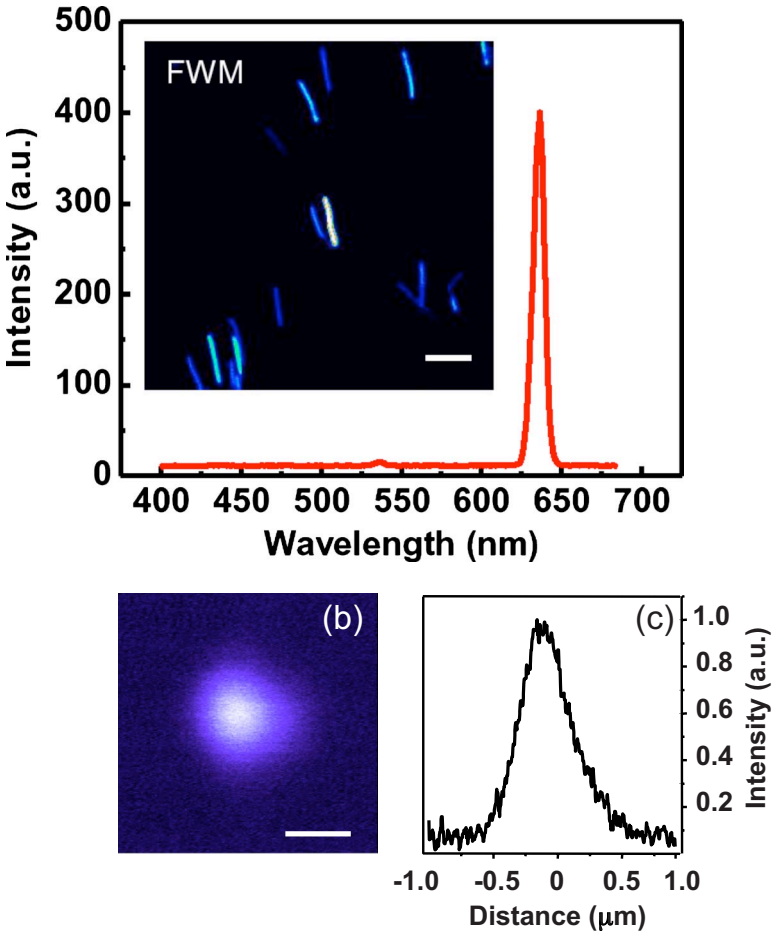


Electronic CARS FWM emission from silicon. (a) FWM from nanowires. The emission maximum from a 40 nm diameter silicon nanowire, illuminated with incident waves $\omega_1$ ($\lambda_1=790$ nm) and $\omega_2$ ($\lambda_2=1018$ nm), coincides with the expected ($\omega_4=2\omega_1-\omega_2$, $\lambda_4=645$ nm) FWM frequency. The inset shows a FWM image of several silicon nanowires acquired in 0.5 s. Scale bar is 2 $\mu$m. Reprinted in part with permission from [115]. Copyright 2009, American Chemical Society. (b) FWM from a 30 nm diameter silicon nanoparticle ($\lambda_1=817$ nm and $\lambda_2=1064$ nm). The particle size is much smaller than the focal volume of the 1.1 NA water immersion lens, enabling an effective point spread function measurement, which provides information about the size and shape of the focal spot. Scale bar is 0.5 $\mu$m. (c) One-dimensional cross section of the measurement in (b). The width of the profile is $\sim$0.40 $\mu$m.

cluding ZnO [134], $TiO_2$ [135], and $CeO_2$ [136], is above 2.0 eV, which implies that these materials are transparent at near-infrared excitation energies. Additional enhancement may thus be expected from multiphoton resonances when these materials are illuminated with ultrafast radiation in the near-infrared range. The effect of the electronic resonant contributions to $\chi^{(3)}$ for several metal oxides is shown in Fig. 9 for the case of THG nonlinear measurements. The $\chi^{(3)}$ shows a clear increase when the bandgap energies approach the three-photon energy (1.96 eV in this case) [124].

Table 3. Third-Order Susceptibility of Several Metal Oxides[a]

| Material | $\chi^{(3)}$ (esu) | $E_g$ (ev) | $\lambda_{edge}$ (nm) | Ref. |
|---|---|---|---|---|
| $\alpha$-$Fe_2O_3$ | $5.8\times10^{-11}$ | 2.1 | 591 | [124] |
| $\gamma$-$Fe_2O_3$ | $2.1\times10^{-11}$ | 2.2 | 564 | [124] |
| $Fe_3O_4$ | $4.0\times10^{-10}$ | 0.3 | 4138 | [124] |
| $Al_2O_3$ | $4.0\times10^{-14}$ | 7.3 | 170 | [125,126] |
| $TiO_2$ (rutile) | $4.0\times10^{-12}$ | 3 | 414 | [127] |
| $SnO_2$ | $3.8\times10^{-12}$ | 3.6 | 345 | [128,129] |
| $In_2O_3$ | $1.7\times10^{-12}$ | 2.9 | 428 | [129,130] |
| $TeO_2$ | $1.4\times10^{-12}$ | 3.37 | 368 | [131] |
| ZnO | $1.4\times10^{-12}$ | 3.37 | 368 | [132] |
| $V_2O_5$ | $1.1\times10^{-11}$ | 2.5 | 497 | [133] |
| $Nb_2O_5$ | $1.3\times10^{-12}$ | 3.2 | 388 | [133] |
| $Ta_2O_5$ | $6.1\times10^{-13}$ | 4.2 | 296 | [133] |

[a]The magnitude of $\chi^{(3)}$ was determined by THG measurements using 1900 nm excitation. The bandgap energy ($E_g$) and the band-edge absorption ($\lambda_{edge}$) wavelength are also given.

In a near-field THG imaging experiment, Johnson *et al.* demonstrated strong $\chi^{(3)}$ signals from ZnO nanowires with diameters in the 50–100 nm range [137]. Similarly, individual titanium oxide nanoparticles with diameters of several tens of nanometers produce very strong FWM signals. Because the size of the nanoparticle is much smaller than the resolution of the FWM microscope, these particles have been used to map out the size and shape of the FWM excitation volume [138]. The magnitude of the FWM signal generated from the $TiO_2$ nanoparticles' response is higher than that of the typical nonresonant third-order response of biological tissues, which permits selective detection of the nanoparticles incorporated into the tissue sample [84,139]. An example is shown in Fig. 10, where the FWM signal from $TiO_2$ nanoparticles is high enough to identify their presence in fish gills [139].

Figure 9

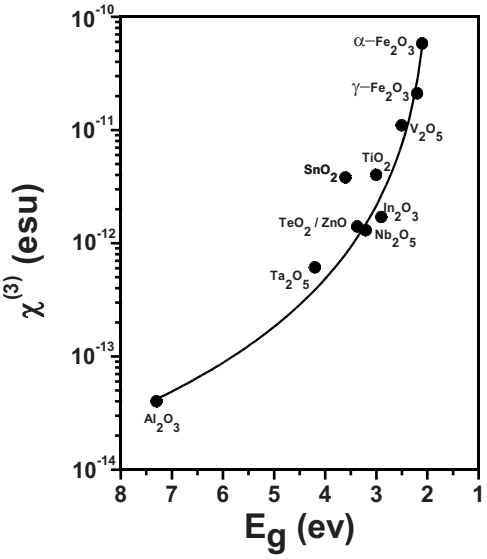


Dispersion of $\chi^{(3)}$ of several metal oxides as a function of the bandgap energy. The solid curve corresponds to a fit based on a phenomenological model for THG generation, as detailed in [127].

Figure 10

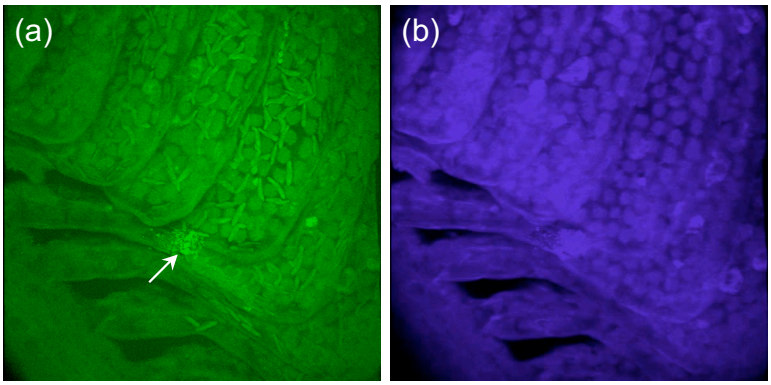


Electronic CARS FWM imaging of $TiO_2$ nanoparticles in fish gill tissue. Fish gills were exposed to $TiO_2$ nanoparticles for a period of one week, resulting in localized clusters of nanoparticles. (a) Three-dimensional projection of the FWM signal from a 150 $\mu$m deep stack in a region of gill tissue containing a large nanoparticles aggregate (white arrow). Detection was in the forward direction. (b) Identical image stack obtained in the epi-direction. Combined laser power of the $\lambda_1$ (924 nm) and $\lambda_2$ (1255 nm) beam was 100 mW. Reprinted in part with permission from [139]. Copyright 2009, Optical Society of America.

Compared with $TiO_2$, the nonlinear susceptibility of iron oxides is markedly higher. Z-scan and THG measurements indicate a $\chi^{(3)}$ larger than $10^{-11}$ esu for nanoscopic $Fe_2O_3$ materials [124,140] and a $\chi^{(3)}$ larger than $10^{-10}$ esu for $Fe_3O_4$ [124]. Such high optical nonlinearities can be exploited for designing efficient FWM probes. FWM imaging studies of iron oxide nanoparticles injected into cells and tissues have shown that such nanomaterials can be readily identified in biological specimens [84].

## 5.3. Semiconducting Quantum Dots

QDs are semiconducting materials that are nanometer sized in all three spatial dimensions. QDs can be prepared from a broad variety of combinations of elements, most notably combinations of group II–VI elements, III–V elements, or IV–VI elements. The size of QDs in the 2–20 nm range is close to or smaller than the exciton Bohr radius of the semiconducting material. Consequently, the optical properties of QDs are largely determined by size confinement of the excitonic excitations, which modifies the electronic band structure typical of bulk semiconductors to more discrete electronic states. In addition to the unique linear optical properties of QDs that follow from the quantum confinement, the nonlinear optical properties of QDs have also attracted considerable attention.

The first FWM experiments on QDs were performed in 1984, which indicated that glasses doped with semiconducting nanocrystallites exhibit a very strong $\chi^{(3)}$ response [51]. These early experiments spurred subsequent theoretical [141] and experimental research focused on the nature and origin of the QD nonlinearities. An important question that has driven research in this field is whether the quantum confinement effects produce an enhanced nonlinearity of the nanomaterial [142]. Even though recent measurements dispute the role of enhanced

nonlinearities attributable to quantum size effects [67,143,144], the complex nonlinear optical properties of QDs are still far from being understood.

Many nonlinear optical experiments on QDs have been devoted to map out the excitation and subsequent ultrafast evolution of the exciton [145]. Despite extensive research, questions remain concerning the coupling of the exciton to other excitons, phonons, and continuum excitations in the QD. A complication in such nonlinear measurements is the difficulty of discriminating the influence of the environment, for instance, coupling to neighboring QDs, from the intrinsic optical properties of the QD. Another complication is the relative heterogeneity among particles in the ensemble. Since the optical properties vary drastically with size, even a moderate dispersion in QD sizes of the ensemble can blur essential information. To avoid such problems, nonlinear optical measurements on single QDs have been carried out. Frequency domain FWM experiments on individual GaAs QDs revealed important information about dephasing mechanisms, which were difficult to observe in ensemble measurements [146]. Furthermore, the free induction decay of the exciton polarization on a single GaAs QD was directly observed with time domain pump–probe measurements using a near-field microscopy approach, which provided clues towards the influence of several Coulombic interactions on the ultrafast exciton dynamics [147]. Third-order nonlinear optical microspectroscopy on single QDs has also been used to shed light on exciton entanglement effects [148].

The experiments discussed above indicate that strong optical signals can be generated from QDs, strong enough to perform nonlinear optical manipulations of fundamental excitations on a single QD. Such measurements are possible because of the intrinsically high nonresonant $\chi^{(3)}$ of semiconducting materials in addition to a direct one-photon resonant excitation of the QD. The nonlinear properties of some common semiconducting QD materials are given in Table 4. The strong $\chi^{(3)}$ response suggests that QD materials are excellent probes for wide range of FWM imaging applications. Using an imaging optical microscope configuration, Masia *et al.* showed that one-photon resonant excitation of CdSe/ZnS QDs produces FWM signals that are indeed more than sufficient for fast imaging applications [18].

Interesting FWM applications could also emerge for QDs that are transparent at the fundamental laser excitation energies while resonant at two-photon excitation energies. Multiphoton excitation of QDs has been used in fluorescence microscopy studies as an efficient means to generate bright signals from fluores-

**Table 4. Third-Order Nonlinear Susceptibility of Types II–VI and III–V Semiconducting Materials[a]**

| Material | Technique | $\chi^{(3)}$ (esu) | $E_g$ (eV) | $\lambda_{edge}$ (nm) | $n_0$ | Ref. |
|---|---|---|---|---|---|---|
| GaAs | THG (1.06 $\mu$m) | $1.4\times10^{-10}$ | 1.35 | 919 | 3.47 | [53,107] |
| CdSe | calculation | $3.0\times10^{-11}$ | 1.74 | 713 | 2.56 | [107,149] |
| CdTe | calculation | $5.4\times10^{-11}$ | 1.44 | 862 | 2.84 | [107,149] |
| ZnS | calculation | $2.0\times10^{-12}$ | 3.54 | 351 | 2.4 | [107,149] |
| ZnSe | THG (1.06 $\mu$m) | $1.2\times10^{-11}$ | 2.58 | 481 | 2.48 | [107,149] |
| GaP | calculation | $2.1\times10^{-11}$ | 2.24 | 554 | 3.2 | [149] |

[a]Magnitudes are for $\chi^{(3)}(-3\omega;\omega,\omega,\omega)$, as determined in a THG experiment. Calculations assume the long wavelength limit ($\hbar\omega\rightarrow 0$ eV, far from bandgap energy). The bandgap energy ($E_g$), band-edge absorption wavelength ($\lambda_{edge}$) and the linear refractive index ($n_0$) are also given.

Figure 11

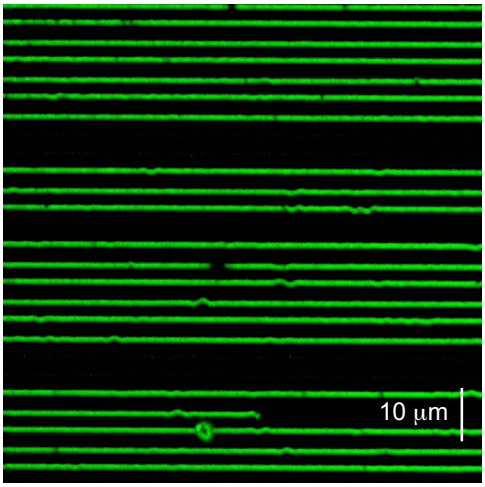


Electronic CARS FWM imaging of semiconducting CdSe nanowires using ps laser pulses. CdSe wires are 330 nm wide, 60 nm high and were lithographically fabricated on a glass cover slip. Details on fabrication can be found in [155]. FWM signals were detected in the epi-direction. The combined laser power of the $\lambda_1$ (817 nm) and $\lambda_2$ (1064 nm) beam was 10 mW.

cent QDs [16], which are particularly useful as labels in biological imaging [150,151]. FWM excitation of QDs potentially has an important advantage over multiphoton excited QDs in cellular and tissue imaging. FWM microscopy of QDs may prove to be less sensitive to blinking, which has limited several fast imaging applications in fluorescence microscopy. So far, two-photon resonant FWM imaging QDs has yet to be demonstrated, but its tentative insensitivity to blinking and photobleaching would extend the use of QDs as bio-labels for studies that require high imaging acquisition rates or sustained signals over longer periods. Recent progress in modeling the two-photon resonance contribution to $\chi^{(3)}$ would, furthermore, facilitate the tailored application of QDs for FWM imaging [67,152–154].

Similar to QDs, semiconducting nanowires, which exhibit nanosized dimensions along transverse axes of the structure but microscopic to macroscopic dimensions along the longitudinal axis, also hold promise as materials with useful FWM imaging applications. An example is shown in Fig. 11, where a CdSe nanowire grid is visualized by using FWM microscopy. Strong signals are observed at low excitation densities of less than 1 MW/cm with excitation energies below the bandgap. The FWM contrast constitutes a promising probe for identifying spatial heterogeneity along the wire, changes in the electronic properties as a function of bias and current, or for examining the material properties during light induced conductivity experiments [155].

## 6. Four-Wave Mixing at Metallic Nanostructures

The optical nonlinearity of bulk metals is several orders of magnitude higher than the nonlinearity of biological materials and most organic matter. Yet the use for bulk metals in nonlinear microscopy is limited owing to their nontranspar-

ency. At the nanoscale, however, the optical properties of several metals are dictated by the presence of surface plasmons, which has opened up many interesting applications for nanometallic structures in nonlinear microscopy. Below we will discuss several examples of nonlinear FWM excitation of surface plasmon polaritons (SPPs) at metallic interfaces and localized surface plasmons at nanoparticles.

## 6.1. Four-Wave Mixing in Metals

To understand the nonlinear optical response from metals, it is useful to separate the nonlinear contribution from the bulk from the contributions stemming from extra resonances at the metal surface. We will first consider the bulk response and then separately discuss the contribution originating from surface resonances.

In the linear regime, the polarization $P(\omega)$ of the metal material due to an incident electric field $E(\omega)$ is

$$P(\omega) = \epsilon_0 \chi^{(1)}(\omega) E(\omega), \tag{11}$$

where $\chi^{(1)}$ is the linear susceptibility. In the weak field limit, the linear susceptibility is related to the dielectric function $\epsilon(\omega) = 1 + 4\pi\chi^{(1)}(\omega)$. For frequencies $\omega$ smaller than the plasma frequency of the metal, the dielectric function is negative. This condition holds for most metals when the incident radiation is in the visible and near-infrared range, and has major consequences for the optical properties of the bulk material.

Assuming an incident plane wave propagating with wave vector $k_{\text{in}}$ along an axis $z$ normal to the metal surface; the resulting electric field in the metal can be found from Maxwell's wave equation as

$$E(z, \omega) = E_0 e^{-ik_m(\omega)z}, \tag{12}$$

where $k_m(\omega) = \omega\sqrt{\epsilon(\omega)}/c$ is the complex wave vector in the material. Because $\epsilon(\omega) < 0$ for visible and near-infrared frequencies, $k_m(\omega)$ is imaginary, and the electric field decays exponentially away from the metal surface. The decay constant is also known as the skin depth of the metal, which is of the order of $\lambda/2\pi$, i.e., a fraction of the optical wavelength. The limited skin depth of the metal has important implications for the generation of third-order nonlinear signals. First, since the amplitude of the electric field in the metal decays within the first few hundred nanometers, a nonlinear polarization of the material is induced predominantly close to the surface, within the range of the metal's skin depth. Second, radiation following from a nonlinear polarization of the material is subject to attenuation because of the nonpropagating character of the emitted wave in the metal. The attenuation of the emitted light is higher for locations away from the metal surface, deeper into the metal. Nonlinear $\chi^{(3)}$ signals from the bulk metal thus originate predominantly from the first $d \sim \lambda/2\pi$ near the metal surface. Unlike the $\chi^{(2)}$ response, which vanishes for the bulk, the $\chi^{(3)}$ response for the metal bulk is nonvanishing. While the $\chi^{(2)}$ response at the metallic surface originates from a region of the order of a lattice constant away from the surface, the third-order nonlinear signal results from dipolar oscillations occurring over a length scale that is evidently much larger than a lattice constant. Hence, the $\chi^{(3)}$ response does not originate solely from dipoles induced at the surface of the metal, as the bulk metal within the entire skin depth volume is also a source of FWM radiation.

The metal's third-order nonlinearity, the source of FWM radiation, is conveniently measured in reflection mode. Reflective-based THG from gold and silver at 1064 nm revealed bulk $\chi^{(3)}$ values of the order of $10^{-11}$ esu [52,53]. The nonlinear properties of several metals are listed in Table 5.

In the case of nanostructured metals, the dimensions of the material are typically comparable with or smaller than the skin depth of the metal. This implies that incident light can relatively effectively penetrate the structure and set up a nonlinear polarization throughout the bulk of the nano-object. Yet the third-order polarization of the bulk alone is insufficient to describe the nonlinear response of the material. The presence of surface plasmon resonances provides an additional contribution to the nonlinear polarization, which often dominates the overall $\chi^{(3)}$ response of the metallic nanostructure. Below we first discuss the nonlinear excitation of SPPs before we focus on the FWM response of metallic nano-objects.

## 6.2. Nonlinear Excitation of Surface Plasmon Polaritons

SPPs are collective electron oscillations that are bound to planar or cylindrical metallic surfaces. These surface resonances are characterized by a wave vector $k^{sp}$ that is directed parallel to the metal surface, forming traveling or standing electromagnetic waves confined to the surface plane [158,159]. The wave vector of the surface plasmon mode at frequency $\omega$ is

$$k^{sp} = (\omega/c)\{\epsilon(\omega)/[\epsilon(\omega) + 1]\}^{1/2}, \tag{13}$$

where $c$ is the speed of light. The momentum of the SPP mode at frequency $\omega$ is higher than that of freely propagating electromagnetic radiation of the same frequency. To excite the SPP mode, incoming light is applied in the form of evanescent waves, which can be achieved in a Kretschmann or Otto total internal reflection configuration of the incident radiation, or through coupling at gratings and nanoscopic defects [160–162].

Linear excitation of SPPs has been the subject of intense research, which has resulted in a broad range of applications in nanoplasmonics. The excitation of SPP modes at planar metal surfaces is particularly relevant for microscopy applications, as SPPs can be readily excited in thin metal films on glass substrates when using high-numerical-objective lenses. As shown by Bouhelier *et al.*, the angular spectrum of a high-numerical-aperture lens contains the wave vectors required for launching counterpropagating SPP in smooth metal films (see Fig. 12) [163]. For our discussion here, we will focus on the nonlinear excitation of SPP modes, an excitation mechanism that has received relatively little attention. Plasmon ex-

**Table 5. Third-Order Nonlinear Susceptibility of Metals**[a]

| Material | Technique | λ (nm) | $\chi^{(3)}$ (esu) | Ref. |
|---|---|---|---|---|
| Au (bulk) | THG | 1064 | $2.4\times10^{-11}$ | [53] |
| Au (thin film) | Z-scan | 532 | $5.1\times10^{-8}$ | [156] |
| Au (10 nm colloids) | DFWM | 532 | $1.5\times10^{-8}$ | [157] |
| Ag (bulk) | THG | 1064 | $1.9\times10^{-11}$ | [53] |
| Ag (7 nm colloids) | DFWM | 400 | $2.4\times10^{-9}$ | [157] |
| Cu (bulk) (THG) | THG | 1064 | $2.1\times10^{-11}$ | [53] |
| Al (bulk) (THG) | THG | 1064 | $1.7\times10^{-10}$ | [53] |

[a]The wavelength of excitation (λ) used in the measurement is also given.

Figure 12

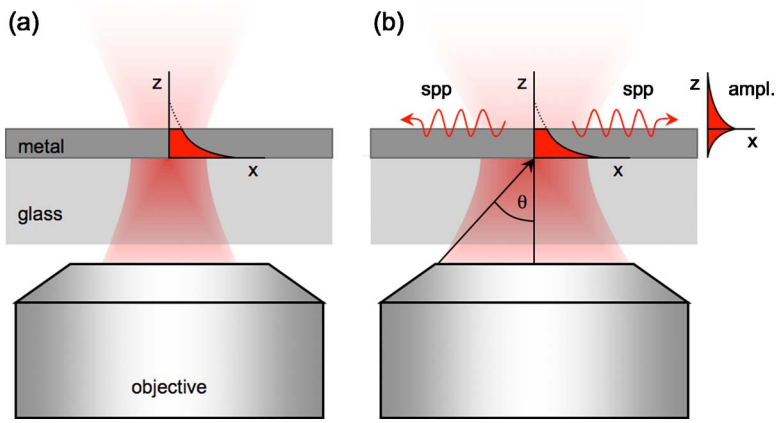


Illuminating a thin metal film with a high-numerical-aperture lens in an inverted microscope configuration. (a) Schematic for low-NA illumination conditions. The incident light is normal to the metal surface and is partially backreflected at the glass/metal interface. In the metal, the electromagnetic field is nonpropagating, and the field amplitude is exponentially decaying along the axial dimension. If the metal film is thinner than the skin depth, part of the light will be transmitted through the film. (b) Schematic for high-NA illumination conditions. If the cone angle of the lens includes the angle needed for coupling to the SPP, counterpropagating surface waves will be launched that will interfere depending on the defocus from the interface.

citation through a nonlinear polarization of the material near the surface was first reported for second-harmonic generation (SHG). In 1974, Simon *et al.* showed that SHG at a silver/air interface can be enhanced through excitation of SPP modes [164]. These observations indicate that, next to the SHG radiation induced in the material at the interface, the involvement of the surface mode increases the overall nonlinear polarization near the interfacial region. The SPP modes were found to modify the SHG emission in two ways. First, the excitation of surface waves at the fundamental frequency provides an enhanced electric field near the interface, which in turn enhances the nonlinear polarization in the interfacial region [165]. Second, under the right phase matching conditions, surface waves at the harmonic frequency are launched [165]. The leakage radiation from the harmonic surface waves can interfere with the other sources of second-harmonic radiation at the interface. By angularly resolving the second-harmonic emission from a gold interface, Palomba and Novotny showed that the contributions from the harmonic surface waves and the interfacial second-harmonic radiation can destructively interfere [166]. These studies show that in the presence of surface modes, the nonlinear emission generated near the metal surface is a complex interplay of regular interfacial emission, plasmon-enhanced interfacial emission, and contributions from higher-order surface waves.

In addition to SHG, excitation of metal SPP modes has also been shown to affect the generation of other nonlinear optical signals at metal surfaces, including FWM. In as early as 1976, De Martini *et al.* predicted theoretically [167] and demonstrated experimentally [168] that surface plasmon waves can be excited at combination frequencies of the incoming light at frequencies $\omega_1$ and $\omega_2$. In this

process, the surface waves at frequencies $\omega_1$ and $\omega_2$ with wave vectors $k_1^{sp}$ and $k_2^{sp}$, respectively, enhance the nonlinear polarization and subsequent emission at FWM frequency $\omega_4 = 2\omega_1 - \omega_2$ in the vicinity of the surface. In addition, a surface wave at frequency $\omega_4$ is launched if wave vector matching is fulfilled at the interface. Similar to SHG generation in thin metal films on glass substrates, interference phenomena between the different sources of radiation at $\omega_4$ may occur depending on the sample geometry and the angle of illumination and detection [166]. Other than SHG, which is intrinsically confined to the interface due to the centrosymmetry of the metal bulk, the FWM radiation originates from a larger region near the interface. The plasmon-mediated FWM emission extends over the penetration depth of the surface plasmon mode into the material and is thus a good probe for the bulk $\chi^{(3)}$. Chen *et al.* used this phenomenon to measure the SPP-enhanced coherent anti-Stokes Raman response from liquid benzene at a silver metal surface, which constitutes the first example of surface-enhanced CARS [169]. In addition to the surface plasmon mediated FWM emission, intrinsic FWM generation in the metal bulk as well as in the glass substrate can contribute to the signal. The work by Chen and coworkers shows that if the experimental configuration is properly chosen, the detected signal is dominated by the SPP-enhanced FWM response near the metal surface. Similar results have been reported for THG at metal surfaces [170].

Recently, Renger *et al.* clearly demonstrated that SPP modes can be nonlinearly excited without launching plasmon modes directly at the frequency of the incident waves [171]. By choosing the incident angles such that only the wave vector associated with the FWM frequency $\omega_4 = 2\omega_1 - \omega_2$ is phase matched with the SPP mode, surface bound modes of frequency $\omega_4$ were generated. This nonlinearly excited evanescent radiation was then coupled with a nanograting to a propagating mode, resulting in fully coherent radiation at the FWM signal frequency [172]. The FWM scheme thus enables free-space excitation of SPP modes, which can be achieved both in thin films and at surfaces of bulk metals.

The nonlinear experiments on smooth and thin metal films performed since the 1970s make clear that the excitation of surface plasmon modes can dominate the FWM response of metals. In particular, upon excitation of SPP modes at $\omega_1$ and $\omega_2$, the amplitude of the electric fields near the surface is increased, enhancing the nonlinear polarization of the material and the subsequent FWM emission from the interfacial region. Similar effects are expected when localized surface plasmon modes are excited, which dominate the optical response of a variety of nanostructured metals, including gold and silver, which will be discussed in the next section.

## 6.3. Nonlinear Excitation of Localized Surface Plasmon Resonances

Similar to metallic interfaces, nanostructured metals exhibit collective electron resonances of conduction electrons. Unlike surface plasmon polaritions on smooth surfaces, which can propagate in the surface plane, the plasmon resonances at the surface of the nanostructure are nonpropagating local waves. Such plasmon resonances are commonly called localized surface plasmons. Although all electrons in the nanosized metal structure oscillate with respect to the atomic lattice, the charges created at the surface provide a surface polarization that is the main restoring force, thus dressing the system with eigenfrequencies. The frequency of the surface plasmon resonances depends strongly on the dielectric function of the metal and on the size and the shape of the structure. For gold and

silver spheres with diameters in the 10–50 nm range, the surface plasmon resonances are found in the visible range of the spectrum.

The evanescent electric field amplitude associated with the plasmon modes is highest near the surface of the metal nanoparticle. The local electric field strength, within a nanometer from the surface, can be very substantial, both inside as well as outside the metal. For gold and silver nanostructures, for instance, the local field amplitude can be several orders of magnitude higher than the amplitude of the driving field. The enhanced local field, in turn, enhances the nonlinear polarization in the metal and provides a source for increased nonlinear emission from the nanostructure.

The enhancement of a field with driving frequency $\omega$ in the vicinity of the metal surface can be expressed in terms of a local field correction factor $L(\omega)$. The correction factor can be determined by solving Maxwell's equations for the illuminated nanostructure and comparing the calculated local electric field near the surface with the incident electric field density. For select shapes of the nanostructure, including spheres [173–175], spheroids, and rectangles [176], analytical solutions for the electric field can be found. A useful analytical model for calculating the local field factor of spheroid-shaped objects was developed by Shen and co-workers and is briefly explained in Box 1. For more complicated shapes of the metal structure, numerical methods such as finite difference time domain methods can be used [177].

Within the framework of Maxwell-Garnett theory [178], the nonlinear polarization in the metal for CARS-type FWM processes can be modeled as

$$P(\omega_4) = L(\omega_4)\epsilon_o\chi^{(3)}(-\omega_4;\omega_1,\omega_1,-\omega_2)\{L(\omega_1)\}^2L^*(\omega_2)E^2(\omega_1)E^*(\omega_2), \tag{14}$$

where $\chi^{(3)}(-\omega_4;\omega_1,\omega_1,-\omega_2)$ is the nonlinear susceptibility of the bulk metal. In this model, the enhanced nonlinear response of the metal nanostructure originates solely from the enhanced local electric field in the metal. In 1983, Chemla *et al.* showed for the first time that the FWM from nanostructured silver was significantly enhanced relative to signals attained from the bulk metal [179]. This enhancement was interpreted as resulting from the enhanced local field inside the silver nanostructures, which is expected to be the dominant enhancement mechanism for silver structures in the 10–100 nm range. However, for smaller particle sizes ($<5$ nm) additional enhancement can be expected from size-dependent changes in the material's nonlinear susceptibility [180]. In 1985, using DFWM measurements, Ricard *et al.* reported values of $\chi^{(3)}$ for silver nanoparticles that were significantly higher than the bulk nonlinear susceptibility of silver [157], which was attributed to a modified dielectric function due to the limited mean free scattering path of the electrons [180,181]. Effective nonlinear susceptibilities of silver as high as $10^{-9}$ esu were measured. Similar effects were observed for nanosized gold [182,183] and copper [184].

As demonstrated by Danckwerts and co-workers, the plasmon-enhanced $\chi^{(3)}(-\omega_4;\omega_1,\omega_1,-\omega_2)$ response is strong enough to generate detectable nonlinear optical signals from single metal nanospheres [80,185]. The feasibility of FWM-based imaging of metallic nanostructures is illustrated in Fig. 13, which depicts the emission spectrum of a single gold nanowire when illuminated with a picosecond (ps) pulse pair $(\omega_1,\omega_2)$. The spectrum shows a broad emission and clearly defined peaks that correspond to frequency combinations of the incident waves. The narrow peaks, whose width matches the convolved spectral width of

Figure 13

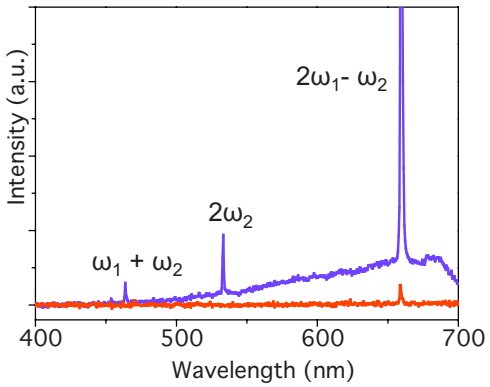


Frequency mixing at a rectangular gold nanowire. Emission spectrum of a single gold nanowire (180 nm wide, 25 nm high) when illuminated with two ps pulses at $\lambda_1$ (817 nm) and $\lambda_2$ (1064 nm). Electronic CARS, SHG and SGF are clearly observed. The blue curve is measured when the laser beams are polarized perpendicular to the long axis of the nanowire (parallel to the traverse surface plasmon mode). The red curve is obtained when the excitation beams are polarized orthogonal to the transverse surface plasmon mode.

the laser pulses, occur at the FWM frequency $2\omega_1 - \omega_2$, the SHG frequency $2\omega_2$, and the sum-frequency generation frequency $\omega_1 + \omega_2$. Other frequency combinations fall outside the spectral range of the detector system. The narrow lines correspond to the plasmon-enhanced third- and second-order coherent response of the metal. The broad emission, on the other hand, results from plasmon-enhanced TPA by the gold, exciting *d*-band electrons to the *sp* band [186]. Subsequent relaxation to the Fermi level produces a broad (incoherent) luminescence, which has been used to probe gold nanostructures in biological imaging applications [187–189].

Using spectral filtering and optimized excitation conditions, the FWM signal can be reliably separated from the two-photon excited fluorescence. Under such conditions, the FWM signal generated in the metal can be used as a direct probe of the local field enhancement in nanostructured metals. This method has been used to map out plasmonic hot spots in structured gold nanowires, as illustrated in Fig. 14 [82]. The FWM signal also forms a convenient probe for gold nanorods dispersed in biological specimens [81]. Other than the two-photon excited fluorescence signal from nanorods, which is determined by the luminescence emission spectrum of the gold material, the FWM emission wavelength can be chosen anywhere in the vicinity of the plasmon absorption band. This allows for selective tuning of the emission wavelength, which can be helpful in multicolor microscopy applications. The selectivity of the FWM response relative to other nonlinear signals generated in gold nanoparticles can be further improved by three-beam excitation and heterodyne detection. Masia *et al.* demonstrated selective visualization of gold nanoparticles associated with secondary antibodies for imaging of organelles in cells (see Fig. 15) [83].

Figure 14

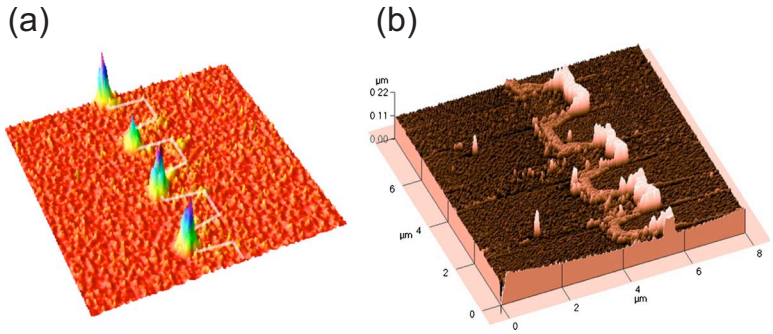


Electronic CARS FWM imaging of gold nanowire structures. (a) FWM image of a zig-zag gold nanowire. Dimensions of the image are 10 $\mu$m $\times$ 10 $\mu$m. (b) Atomic force microscopy image of the zig-zag wire. The tall plateaus are $\sim$80 nm high, and the shallow plateaus are $\sim$20 nm high. Note that the strongest FWM signals are obtained from the shallow plateaus, indicating much stronger local fields in those areas.

## 6.4. Plasmon-Enhanced CARS

The strong FWM signal from nanostructured metals results predominantly from the plasmon-enhanced local fields in the metal. The observation that the field enhancement inside the metal is sufficient to mediate a detectable signal through the $\chi^{(3)}$ of the material suggests that the local field *outside* the nanostructure may induce an appreciable third-order response from molecules or materials in the direct vicinity of the metal's surface. When applied to molecules tethered to the surface, an enhanced molecular response can be expected in a vibrationally resonant CARS excitation scheme. Such an experiment would constitute a nonlinear analog of the surface-enhanced Raman scattering technique [193–197].

Although both surface-enhanced Raman scattering and surface-enhanced CARS (SE-CARS) involve a vibrational Raman interaction at a surface-plasmon active surface, several important differences between the techniques exist. First, the CARS response is composed of both the electronic FWM response from the metal nanosubstrate and the third-order response of the molecule. The electronically enhanced $\chi^{(3)}$ of the metal is generally larger than the vibrationally resonant $\chi^{(3)}$ of the molecule, and the metal volume that partakes in FWM signal generation is typically much larger than the number density of molecules tethered to the surface. This implies that an electronic FWM signal can be expected that is many orders of magnitude stronger than the molecular CARS response. When the CARS excitation scheme is used, suppression of the electronic background may thus be necessary, which can be achieved, for instance, with polarization-sensitive detection [198,199], time-resolved detection [200] or phase-sensitive detection techniques [201,202]. Second, the CARS signal is coherent, whereas the surface-enhanced Raman scattering emission is incoherent. Note that, because of the coherence, the electronic FWM from the metal may actually amplify the molecular CARS field in a homodyne matter. Third, the heating characteristics of the metal when illuminated with ultrafast pulses are different from the heating mechanisms under continuous wave illumination. Experiments indicate an increased photothermal heating of the nanoscopic metal when shorter pulses are used at constant fluence rates [203,204]. An example is

Figure 15

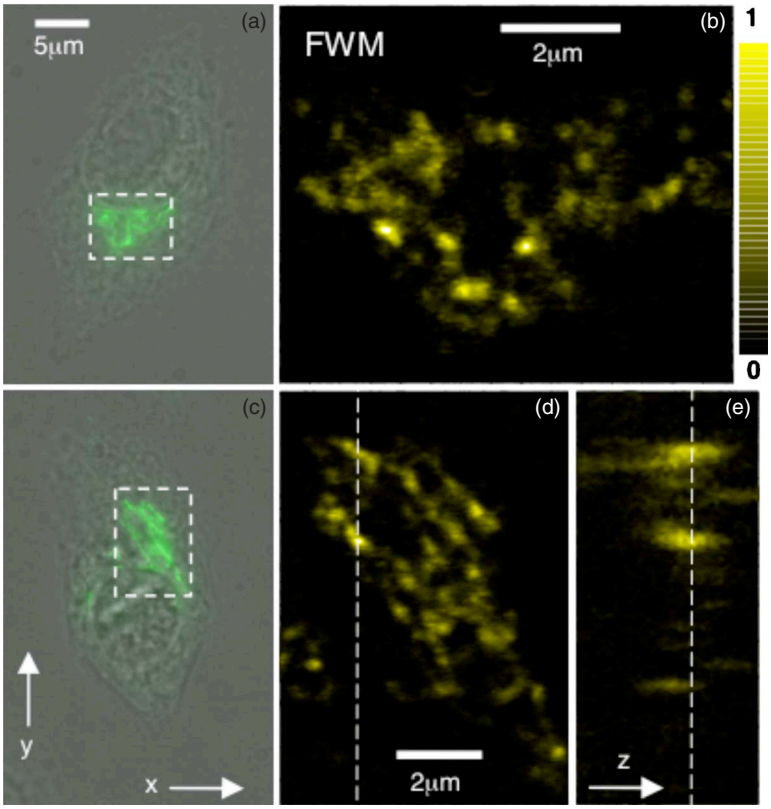


Images of cells (HepG2) in which the Golgi apparatus is stained with an Alexa488 fluorescent immunostain, and a secondary antibody with gold nanoparticles. (a) Epifluorescence image overlaid with a phase contrast image of a cell labeled with 10 nm diameter gold nanoparticles. (b) Close up of the Golgi apparatus based on electronic FWM contrast of the gold nanoparticle of the dashed square area in (a). (c) Epifluorescence image overlaid with a phase contrast image of a cell labeled with 5 nm diameter gold nanoparticles. (d) Close up of the Golgi apparatus based on electronic FWM contrast of the gold nanoparticle of the dashed square area in (c). (e) *yz* image taken at the dashed line in (d). Reprinted with permission from [83]. Copyright 2009, Optical Society of America.

shown in Fig. 16, where photothermal melting introduces shape changes to the nanoparticles [205].

Evidence of SE-CARS effects have come from experiments on SPP excitation at smooth silver surfaces [169], silver colloidal solutions [206], gold particles embedded in a polymer host [207] and from tip-enhanced FWM on DNA clusters [208]. Although the detailed mechanism that underlies the vibrational SE-CARS signal is currently poorly understood, the reported experiments show that, under optimized conditions, SE-CARS experiments may be used to interrogate the nonlinear vibrational response of low-density molecular samples.

Figure 16

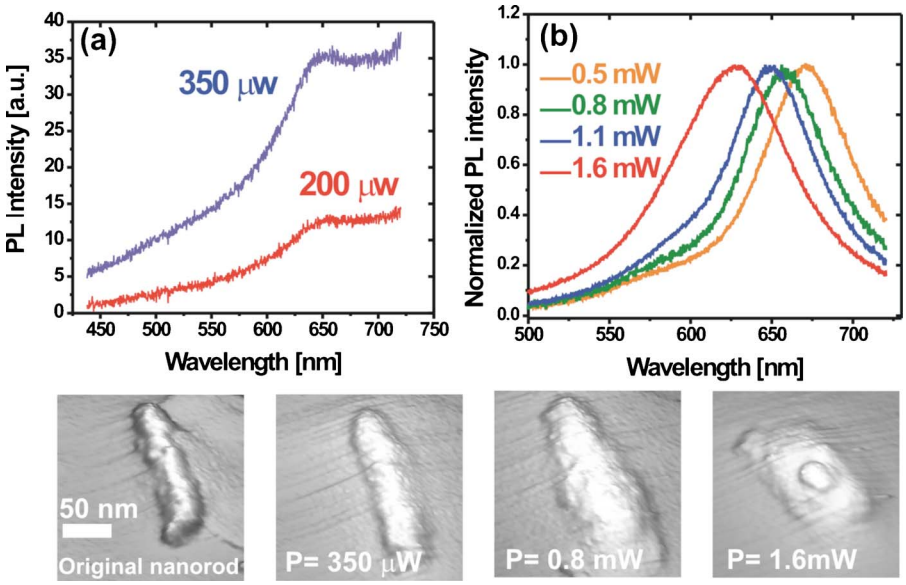


Photothermal heating of gold nanorods when illuminated with femtosecond radiation. (a) Modification of the two-photon excited fluorescence emission spectra of a single gold nanorod (aspect ratio 3.3) with increasing average excitation power. (b) Shift in the photoluminescence with increasing excitation power for the same nanorod, indicating a change in the morphological shape of the particle as shown in the series of AFM images. Reprinted with permission from [205]. Copyright 2005, the American Physical Society (http://prl.aps.org/abstract/PRL/v95/i26/e267405).

## 7. Four-Wave-Mixing Signals from Molecular Systems

Similar to metallic and inorganic nanomaterials, nanostructures composed of molecular building blocks can have high third-order optical nonlinearities. Much research has been devoted to characterizing and optimizing the nonlinear optical response of organic molecules and polymers [209]. Numerous organic microsized and nanosized crystals with large third-order nonlinearities have been synthesized [210–212]. For our discussion here we will focus on the possibility of generating detectable $\chi^{(3)}$ signals from systems as small as single molecules.

Recent advances in single-molecule spectroscopy have consolidated the notion that probing molecular systems one at a time reveals important information about stochastic dynamics that would otherwise remain hidden in ensemble-averaged experimental observables [213–215]. In particular, single-molecule fluorescence methods have successfully contributed to the fundamental understanding of conformational dynamics of enzymes and macromolecules down to the microsecond time scales [216–218]. Such measurements are facilitated by the strong optical response of the fluorescence probing process, which can be conducted with quantum efficiencies approaching 1.

*Box 1. A simple model based on the lightning rod effect can be used to qualitatively understand the FWM dependence on the aspect ratio of the metallic nanostructure. In the lightning rod model, the local field correction factor is factored into a material-dependent surface plasmon correction factor $L_{sp}(\omega)$ and a lightning rod factor $L_{LR}$, which depends on the aspect ratio $(a,b)$ of the nanostructure alone [190–192]:*

$$L(\omega) = L_{sp}(\omega) L_{LR}. \tag{B.1}$$

*The lightning rod factor describes the concentration of the field as function of geometry and plays an important role in determining the magnitude of the optical enhancement. Analytical expressions for the local field correction factor can be obtained if the nanostructure is modeled as an elliptical spheroid. Within this assumption, the local field correction factors are written as*

$$L_{sp}(\omega) = \left[ \epsilon_m(\omega) - 1 + \frac{1}{A}\left\{ 1 + i\frac{4\pi^2 V}{3\lambda^3}(1 - \epsilon_m(\omega)) \right\} \right]^{-1},$$

$$L_{LR} = 1/A, \tag{B.2}$$

*where $\omega$ is the photon frequency, $\epsilon_m(\omega)$ is the complex permittivity of the metal, $V$ is the volume of the nanostructure that is illuminated, and $\lambda$ is the wavelength of the incident light. With the laser light polarized along the a axis of the wire, the depolarization factor $A$ is given as*

$$A = \frac{ab^2}{2}\int_0^\infty \frac{ds}{(s+a^2)^{3/2}\cdot(s+b^2)}. \tag{B.3}$$

The fluorescence process has also been used as the probing event in time-resolved pump–probe measurements to uncover the ultrafast dynamics of single molecules [219]. The single-molecule approach circumvents ensemble average related contributions to excited state dynamics (inhomogeneous broadening) and is expected to produce new information about how stochastic fluctuations affect single quantum systems on the ultrafast time scales. Time-resolved third-order optical spectroscopy is the preferred method for probing quantum coherences in molecular systems. Nonetheless, the sensitivity of $\chi^{(3)}$-based techniques is many orders of magnitude less than the sensitivities attained in fluorescence detection techniques. With a material response of $\chi^{(3)} \sim 10^{-14}$ esu under electronically nonresonant conditions, the excitation intensities needed to induce nonlinear radiation from systems as small as single molecules impose experi-

mental limitations in terms of photodamage of the compound and substrate. A stronger, nondestructive material response is required at lower excitation densities to bring single molecules into the realm of feasible FWM targets. One route to this goal is to select molecules with a very high $\chi^{(3)}$ response, aided by the presence of electronic resonances.

By using a broadband femtosecond laser tuned into one-photon resonance with the electronic transitions of a strongly absorbing chromophore, Min *et al.* were able to generate electronic FWM signals from molecular solutions in the 1 $\mu$M range using sensitive heterodyne detection [220]. As shown in Fig. 17, this FWM approach is capable of visualizing endogenous chromophores in biological materials, such as hemoglobin and cytochrome *c*, without the use of fluorescent labels. In this triply resonant scheme, as few as 50 molecules could be detected in the microscopic probing volume. These results indicate that $\chi^{(3)}$-based measurements on strongly resonant molecular systems can approach the detection sensitivities needed for single-molecule FWM measurements.

Recent experiments have shown that electronically resonant FWM measurements can be used to study the nonlinear optical response of individual single-walled carbon nanotubes. Carbon nanotubes are quasi-one-dimensional molecular systems with enhanced electronic properties along the main tube axis that are absent in bulk carbon materials [221]. The enhanced delocalized electronic excitations dress carbon nanotubes with a very high $\chi^{(3)}$ [222]. Degenerate FWM experiments on films and dilute solutions indicate a third-order nonlinearity higher than $10^{-11}$ esu on the nanosecond time scale [223,224]. FWM imaging experiments indicate that under electronically resonant conditions, detectable signals

Figure 17

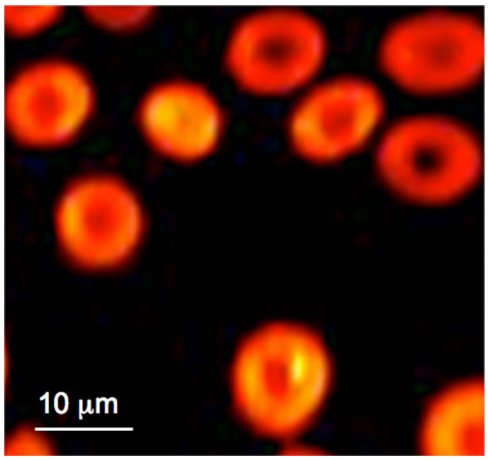


Electronically resonant FWM imaging of red blood cells. A broad continuum was used for excitation, which was truncated at the blue side of the spectrum. Difference-frequency mixing components within the band induce electronic CARS-type blueshifted components that can be spectrally isolated and detected. Strong signals are observed when the laser spectrum in this (nondegenerate) FWM scheme is tuned to near-resonance with the *Q* band of (de-)oxyhemoglobin. The donut shape of red blood cells is clearly illustrated. Reprinted in part with permission from [220]. Copyright 2009, American Chemical Society.

can be observed from individual nanotubes dispersed on a quartz substrate [225]. In these experiments, ps pulses were used to visualize the carbon nanotubes through a dual-color ($\omega_1, \omega_2$) CARS excitation scheme. Figure 18 shows that the FWM signal is maximized when the polarization of the excitation fields is aligned with the long axis of the nanotube, in the direction where maximum electronic enhancement is expected. Even stronger FWM signals are expected when femtosecond excitation would be used in such measurements of carbon nanotubes. These experiments show that time-resolved third-order optical measurements, which have been used to examine the ultrafast dynamics of electronic excitations in nanotube ensembles [226–229], could possibly be conducted on a single-nanotube level.

With single-molecule $\chi^{(3)}$ measurements on the horizon, several fundamental questions concerning nonlinear light–matter interactions will need to be answered in order to model this emerging class of experiments. Recent theoretical work has brought forth the notion that the $\chi^{(3)}$ quantity is not a good descriptor of the material response when the nonlinear optical signal is deduced from one-electron transitions on a single molecule [230]. A description based on quantized electric field interactions was found to be more useful for interpreting third-order nonlinear experiments of single-molecular systems [231,232].

## 8. Conclusions

Although FWM techniques have been around since the dawn of nonlinear optical spectroscopy, the recent application of the FWM scheme as a contrast mechanism in microscopy has opened up new opportunities for investigating the nonlinear properties of microscopic and nanoscopic structures. The FWM technique, in the form of a CARS excitation scheme, has gained popularity as a vibrational imaging tool in biology and materials sciences. It can be expected that by expanding the FWM palette with contrast based on electronic resonances, a new domain of materials will be opened up for examination with FWM imaging techniques.

Figure 18

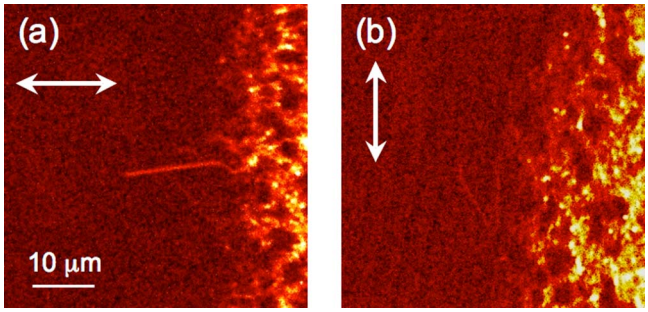


Electronically resonant FWM imaging of carbon nanotubes. (a) FWM image of an individual carbon nanotube of a 3.9 nm multiwalled nanotube. The polarization direction of the incident beams is indicated by the white arrow. A strong signal is observed when the polarization of the excitation beams is aligned with the enhanced electronic excitations along the long axis of the nanotube. (b) FWM image of the same nanotube when the beam polarization is orthogonal to the long axis of the nanotube. Without direct excitation of the enhanced electronic transitions in the nanotube, no discernible FWM signal is observed.

Nonlinear optical tools are particularly relevant to the development and application of nanomaterials. Many nanomaterials exhibit strong optical nonlinearities due to quantum confinement effects or strong electronic resonances. Such enhanced optical properties enable the detection of nanostructures with FWM techniques on a single-particle level, which facilitates detailed studies aimed at understanding the electronic properties of nanomaterials. FWM measurements on individual nanostructures will be important for the characterization of the relationships between magnitude of $\chi^{(3)}$ and the shape and size of the structure. Time-resolved FWM studies provide avenues for examining the ultrafast dynamics of excitations of single nanoparticles, which, without the effects of ensemble averaging, has the potential to establish fundamental correlations between dephasing dynamics and phonon coupling, exciton–exciton coupling, lattice defects, and morphological factors. Ultrafast FWM experiments may also play a role in determining the mechanisms of photoinduced electron transfer between nanostructures and their surroundings, which is directly relevant to the fabrication of nanomaterial-based solar cells.

The unique nonlinear optical properties of nanomaterials can be exploited in a variety of applications. Several nanostructures, including semiconducting QDs and metallic particles, have already found their way as efficient FWM active markers in biological imaging studies. The nonphotobleaching character of such FWM probes makes these materials ideal candidates for sustained biomedical imaging applications [36]. In addition, several FWM processes, including CARS, provide a mechanism for synthesizing spectrally shifted tunable radiation at nanostructures. This form of controlled and localized frequency generation has been proposed as a light source for near-field imaging applications [80,185]. Finally, the application of nonlinear nanomaterials in functional devices is highly promising. For instance, several nanoengineered structures have been proposed as nonlinear elements in light-based computational circuits.

FWM microscopy is a relatively new field, and its application to nanomaterials is still in its infancy. Nonetheless, as illustrated by the examples in this review, the combination of single-particle sensitivity and the ability to tune into specific material properties make the FWM approach particularly promising for examining nanostructures. The studies summarized in this work are undoubtedly just a prelude to a more extensive role for FWM techniques in nanomaterial research.

## Acknowledgments

This work was supported by the National Science Foundation (NSF) Center on Chemistry at the Space-Time Limit at the University of California, Irvine (CHE-0533162), and by NSF grant CHE-0847097. We thank Sheng-shin Kung and Reginald Penner for provision of the CdSe nanowires. We are grateful to Desiré Whitmore for carefully reading the manuscript.

## References

1. A. Rogach, ed., *Semiconductor Nanocrystal Quantum Dots* (Springer, 2008).
2. S. A. Maier, *Plasmonics: Fundamentals and Applications* (Springer, 2007).
3. Lord Rayleigh, "On the theory of optical images with special reference to

the microscope," Philos. Mag. **5**, 167–195 (1896).
4. M. J. Rust, M. Bates, and X. Zhuang, "Sub-diffraction-limit imaging by stochastic optical reconstruction microscopy (STORM)," Nat. Methods **3**, 793–796 (2006).
5. S. W. Hell, "Far-field optical nanoscopy," Science **316**, 1153–1158 (2007).
6. E. Betzig, G. H. Patterson, R. Sougrat, O. W. Lindwasser, S. Olenych, J. S. Bonifacino, M. W. Davidson, J. Lippincott-Schwartz, and H. F. Hess, "Imaging intracellular fluorescent proteins at nanometer resolution," Science **313**, 1642–1645 (2006).
7. K. Imura, T. Nagahara, and H. Okamoto, "Plasmon mode imaging of single gold nanorods," J. Am. Chem. Soc. **126**, 12730–12731 (2004).
8. K. Imura, T. Nagahara, and H. Okamoto, "Near-field optical imaging of plasmon modes in gold nanorods," J. Chem. Phys. **122**, 154701–154705 (2005).
9. Q. Xu, J. Bao, F. Capasso, and G. M. Whitesides, "Surface plasmon resonances of free-standing gold nanowires fabricated using nanoskiving," Angew. Chem. Int. Ed. **45**, 3631–3635 (2006).
10. L. J. Sherry, S. H. Chang, G. C. Schatz, R. P. Van Duyne, B. J. Wiley, and Y. Xia, "Localized surface plasmon resonance spectroscopy of single silver nanocubes," Nano Lett. **5**, 2034–2038 (2005).
11. P. Michler, A. Imamo, M. D. Mason, P. J. Carson, G. F. Strouse, and S. K. Buratto, "Quantum correlation among photons from a single quantum dot at room temperature," Nature **406**, 968–970 (2000).
12. K. T. Shimizu, R. G. Neuhauser, C. A. Leatherdale, S. A. Empedocles, W. K. Woo, and M. G. Bawendi, "Blinking statistics in single semiconductor nanocrystal quantum dots," Phys. Rev. B **63**, 205316 (2001).
13. R. Antoine, P. F. Brevet, H. H. Girault, D. Bethell, and D. Schiffrin, "Surface plasmon enhanced non-linear optical response of gold nanoparticles at the air-toluene interface," Chem. Commun. **1997**(19), 1901–1902 (1997).
14. A. Bouhelier, M. Beversluis, A. Hartschuh, and L. Novotny, "Near-field second-harmonic generation induced by local field enhancement," Phys. Rev. Lett. **90**, 013903 (2003).
15. M. Lippitz, M. A. v. Dijk, and M. Orrit, "Third-harmonic generation from single gold nanoparticles," Nano Lett. **5**, 799–802 (2005).
16. D. R. Larson, W. R. Zipfel, R. M. Williams, S. W. Clark, M. P. Bruchez, F. W. Wise, and W. W. Webb, "Water-soluble quantum dots for multiphoton fluorescence imaging *in vivo*," Science **300**, 1434–1436 (2003).
17. X. Michalet, S. Weiss, and M. Jäger, "Single-molecule fluorescence studies of protein folding and conformational dynamics," Chem. Rev. (Washington, D.C.) **106**, 1785–1813 (2006).
18. F. Masia, W. Langbein, and P. Borri, "Multiphoton microscopy based on four-wave mixing of colloidal quantum dots," Appl. Phys. Lett. **93**, 021114 (2008).
19. M. D. Duncan, J. Reintjes, and T. J. Manuccia, "Scanning coherent anti-Stokes Raman microscope," Opt. Lett. **7**, 350–352 (1982).
20. A. Zumbusch, G. Holtom, and X. S. Xie, "Vibrational microscopy using coherent anti-Stokes Raman scattering," Phys. Rev. Lett. **82**, 4142–4145 (1999).
21. P. D. Maker and R. W. Terhune, "Study of optical effects due to an induced polarization third order in the electric field strength," Phys. Rev. **137**, A801–A818 (1965).
22. J. X. Cheng and X. S. Xie, "Coherent anti-Stokes Raman scattering micros-

copy: instrumentation, theory and applications," J. Phys. Chem. B **108**, 827–840 (2004).
23. C. L. Evans and X. S. Xie, "Coherent anti-Stokes Raman scattering microscopy: chemical imaging for biology and medicine," Annu. Rev. Anal. Chem. **1**, 883–909 (2008).
24. A. Volkmer, "Vibrational imaging and microspectroscopies based on coherent anti-Stokes Raman scattering microscopy," J. Phys. D **38**, R59–R81 (2005).
25. E. Ploetz, S. Laimgruber, S. Berner, W. Zinth, and P. Gilch, "Femtosecond stimulated Raman microscopy," Appl. Phys. B **87**, 389–393 (2007).
26. C. W. Freudiger, W. Min, B. G. Saar, S. Lu, G. R. Holtom, C. He, J. C. Tsai, J. X. Kang, and X. S. Xie, "Label-free biomedical imaging with high sensitivity by stimulated Raman scattering microscopy," Science **322**, 1857–1861 (2008).
27. E. O. Potma, W. P. de Boeij, and D. A. Wiersma, "Femtosecond dynamics of intracellular water probed with nonlinear Kerr effect microspectroscopy," Biophys. J. **80**, 3019–3024 (2001).
28. J. A. Armstrong, N. Bloembergen, J. Ducuing, and P. S. Pershan, "Interactions between light waves in a nonlinear dielectric," Phys. Rev. **127**, 1918–1939 (1962).
29. S. A. J. Druet and J. P. E. Taran, "CARS spectroscopy," Prog. Quantum Electron. **7**, 1–72 (1981).
30. H. Lotem, R. T. Lynch, and N. Bloembergen, "Interference between Raman resonances in four-wave difference mixing," Phys. Rev. A **14**, 1748–1755 (1976).
31. S. A. J. Druet, B. Attal, T. K. Gustafson, and J. P. Taran, "Electronic resonance enhancement of coherent anti-Stokes Raman scattering," Phys. Rev. A **18**, 1529–1557 (1978).
32. R. T. Lynch and H. Lotem, "Two-photon absorption measurements in organic liquids via nonlinear light mixing spectroscopy," J. Chem. Phys. **66**, 1905–1913 (1977).
33. S. Maeda, T. Kamisuki, and Y. Adachi, "Condensed phase CARS," in *Advances in Nonlinear Spectroscopy*, R. J. H. Clark and R. E. Hester, eds. (Wiley, 1988), pp. 253–297.
34. T. Fujii, A. Kamata, M. Shimizu, Y. Adachi, and S. Maeda, "Two-photon absorption study of 1,3,5-hexatriene by CARS and CSRS," Chem. Phys. Lett. **115**, 369–372 (1985).
35. M. L. Shand and R. R. Chance, "Third-order nonlinear mixing in polydiacetylene solutions," J. Chem. Phys. **69**, 4482–4486 (1978).
36. X. Liu, W. Rudolph, and J. L. Thomas, "Photobleaching resistance of stimulated parametric emission in microscopy," Opt. Lett. **34**, 304–306 (2009).
37. X. Liu, W. Rudolph, and J. L. Thomas, "Characterization and application of femtosecond infrared stimulated parametric emission microscopy," J. Opt. Soc. Am. B **27**, 787–795 (2010).
38. K. Isobe, S. Kataoka, R. Murase, W. Watanabe, T. Higashi, S. Kawakami, S. Matsunaga, K. Fukui, and K. Itoh, "Stimulated parametric emission microscopy," Opt. Express **14**, 786–793 (2006).
39. H. M. Dang, G. Omura, T. Umano, M. Yamagiwa, S. Kajiyama, Y. Ozeki, K. Itoh, and K. Fukui, "Label-free imaging by stimulated parametric emission microscopy reveals a differnce in hemoglobin distribution between live and fixed erythrocytes," J. Biomed. Opt. **14**, 040506 (2009).
40. R. F. Begley, A. B. Harvey, and R. L. Byer, "Coherent anti-Stokes Raman

spectroscopy," Appl. Phys. Lett. **25**, 387–390 (1974).
41. R. W. Hellwarth, "Third-order optical susceptibilities of liquids and solids," in *Prog. Quantum Electron.*, J. H. Sanders and S. Stenholm, eds. (Pergamon, 1977), pp. 1–68.
42. L. Li, H. Wang, and J. X. Cheng, "Quantitative coherent anti-Stokes Raman scattering imaging of lipid distribution in coexisting domains," Biophys. J. **89**, 3480–3490 (2005).
43. E. O. Potma and X. S. Xie, "Detection of single lipid bilayers with coherent anti-Stokes Raman scattering (CARS) microscopy," J. Raman Spectrosc. **34**, 642–650 (2003).
44. C. L. Evans, E. O. Potma, M. Puoris'haag, D. Côté, C. P. Lin, and X. S. Xie, "Chemical imaging of tissue *in vivo* with video-rate coherent anti-Stokes Raman scattering microscopy," Proc. Natl. Acad. Sci. U.S.A. **102**, 16807–16812 (2005).
45. E. O. Potma, X. S. Xie, L. Muntean, J. Preusser, D. Jones, J. Ye, S. R. Leone, W. D. Hinsberg, and W. Schade, "Chemical imaging of photoresists with coherent anti-Stokes Raman scattering (CARS) microscopy," J. Phys. Chem. B **108**, 1296–1301 (2004).
46. A. Voroshilov, G. W. Lucassen, C. Otto, and J. Greve, "Polarization-sensitive resonance CSRS of deoxy- and oxyheamoglobin," J. Raman Spectrosc. **26**, 443–450 (1995).
47. A. Voroshilov, C. Otto, and J. Greve, "On the coherent vibrational phase in polarization sensitive resonance CARS spectroscopy of copper tetraphenylporphyrin," J. Chem. Phys. **106**, 2589–2598 (1997).
48. L. A. Carreira, T. C. Maguire, and T. B. Malloy, "Excitation profiles of the coherent anti-Stokes resonance Raman spectrum of $\beta$-carotene," J. Chem. Phys. **66**, 2621–2626 (1977).
49. W. Min, S. Lu, G. R. Holtom, and X. S. Xie, "Triple-resonance coherent anti-Stokes Raman scattering microspectroscopy," ChemPhysChem **10**, 344–347 (2009).
50. R. K. Jain and J. B. Klein, "Degenerate four-wave mixing near the band gap of semiconductors," Appl. Phys. Lett. **35**, 454–456 (1979).
51. R. K. Jain and R. C. Lind, "Degenerate four-wave mixing in semiconductor-doped glasses," J. Opt. Soc. Am. **73**, 647–653 (1983).
52. N. Bloembergen, W. K. Burns, and M. Matsuoka, "Reflected third harmonic generated by picosecond laser pulses," Opt. Commun. **1**, 195–198 (1969).
53. W. K. Burns and N. Bloembergen, "Third-harmonic generation in absorbing media of cubic or isotropic symmetry.," Phys. Rev. B **4**, 3437–3450 (1971).
54. J. J. Wynne, "Optical third-order mixing in GaAS, Ge, Si and InAs," Phys. Rev. **178**, 1295–1303 (1969).
55. F. Kajzar and J. Messier, "Third-harmonic generation in liquids," Phys. Rev. A **32**, 2352–2363 (1985).
56. G. R. Meredith, B. Buchalter, and C. Hanzlik, "Third-order optical susceptibility determination by third-harmonic generation," J. Chem. Phys. **78**, 1533–1542 (1983).
57. R. Barille, L. Canioni, L. Sager, and G. Rivoire, "Nonlinearity measurements of thin films by third harmonic generation microscopy," Phys. Rev. E **66**, 067602 (2002).
58. V. Shcheslavskiy, G. Petrov, and V. V. Yakovlev, "Nonlinear optical susceptibility measurements of solutions using third-harmonic generation on the interface," Appl. Phys. Lett. **82**, 3982–3984 (2003).

59. J. Wang, M. Sheik-Bahae, A. A. Said, D. J. Hagan, and E. W. Van Stryland, "Time-resolved Z-scan measurements of optical nonlinearities," J. Opt. Soc. Am. B **11**, 1009–1017 (1994).
60. P. N. Butcher and D. Cotter, *The Elements of Nonlinear Optics* (Cambridge University Press, 1990).
61. R. P. Davis, A. J. Moad, G. S. Goeken, R. D. Wampler, and G. J. Simpson, "Selection rules and symmetry relations for four-wave mixing measurements of uniaxial assemblies," J. Phys. Chem. B **112**, 5834–5848 (2008).
62. D. L. Mills, *Nonlinear Optics* (Springer-Verlag, 1991).
63. R. W. Boyd, *Nonlinear Optics* (Academic, 2003).
64. D. Débarre and E. Beaurepaire, "Quantitative characterization of biological liquids for third-harmonic generation microscopy," Biophys. J. **92**, 603–612 (2007).
65. U. Gubler and C. Bosshard, "Optical third-harmonic generation of fused silica in gas atmosphere: absolute value of the third-order harmonic nonlinear optical susceptibility $\chi^{(3)}$," Phys. Rev. B **61**, 10702–10710 (2000).
66. G. R. Meredith, B. Buchalter, and C. Hanzlik, "Third-order susceptibility determination by third harmonic generation. II," J. Chem. Phys. **78**, 1543–1551 (1983).
67. D. N. Christodoulides, I. C. Khoo, G. J. Salamo, G. I. Stegeman, and E. W. Van Stryland, "Nonlinear refraction and absorption: mechanisms and magnitudes," Adv. Opt. Photon. **2**, 60–200 (2010).
68. B. Richards and E. Wolf, "Electromagnetic diffraction in optical systems II: structure of the image field in an aplanatic system," Proc. R. Soc. London, Ser. A **253**, 358–379 (1959).
69. L. Novotny and B. Hecht, *Principles of Nano-optics* (Cambridge University Press, 2006).
70. S. Feng and H. G. Winful, "Physical origin of the Gouy phase shift," Opt. Lett. **26**, 485–487 (2001).
71. L. G. Gouy, "Sur une propriété nouvelle des ondes lumineuses," C. R. Acad. Sci. Paris **110**, 1251–1253 (1890).
72. G. C. Bjorklund, "Effects of focusing on the third-order nonlinear process in isotropic media," IEEE J. Quantum Electron. **QE-11**, 287–296 (1975).
73. J.-X. Cheng, A. Volkmer, and X. S. Xie, "Theoretical and experimental characterization of coherent anti-Stokes Raman scattering microscopy," J. Opt. Soc. Am. B **19**, 1363–1375 (2002).
74. E. O. Potma, W. P. d. Boeij, and D. A. Wiersma, "Nonlinear coherent four-wave mixing in optical microscopy," J. Opt. Soc. Am. B **17**, 1678–1684 (2000).
75. J.-X. Cheng and X. S. Xie, "Green's function formulation for third-harmonic generation microscopy," J. Opt. Soc. Am. B **19**, 1604–1610 (2002).
76. D. Débarre, N. Olivier, and E. Beaurepaire, "Signal epidetection in third-harmonic generation microscopy of turbid media," Opt. Express **15**, 8913–8924 (2007).
77. Y. Barad, H. Eisenberg, M. Horowitz, and Y. Silberberg, "Nonlinear scanning laser microscopy by third harmonic generation," Appl. Phys. Lett. **70**, 922–924 (1997).
78. S. W. Chu, I. H. Chen, T. M. Liu, P. C. Chen, C. K. Sun, and B. L. Lin, "Multimodal nonlinear spectral microscopy based on a femtosecond Cr:forsterite laser," Opt. Lett. **26**, 1909–1911 (2001).
79. A. C. Millard, P. W. Wiseman, D. N. Fittinghoff, K. R. Wilson, J. A. Squier,

and M. Müller, "Third-harmonic generation microscopy by use of a compact, femtosecond fiber laser source," Appl. Opt. **38**, 7393–7397 (1999).
80. M. Danckwerts and L. Novotny, "Optical frequency mixing at coupled gold nanoparticles," Phys. Rev. Lett. **98**, 026104 (2007).
81. Y. Jung, H. Chen, L. Tong, and J. X. Cheng, "Imaging gold nanorods by plasmon-resonance-enhanced four-wave mixing," J. Phys. Chem. C **113**, 2657–2663 (2009).
82. H. Kim, D. K. Taggart, C. Xiang, R. M. Penner, and E. O. Potma, "Spatial control of coherent anti-Stokes emission with height-modulated gold zigzag nanowires," Nano Lett. **8**, 2373–2377 (2008).
83. F. Masia, W. Langbein, P. Watson, and P. Borri, "Resonant four-wave-mixing of gold nanoparticles for three-dimensional cell microscopy," Opt. Lett. **34**, 1816–1818 (2009).
84. Y. Zheng, G. Holtom, and S. Colson, "Multichannel multiphoton imaging of metal oxides nanoparticles in biological systems," Proc. SPIE **5323**, 390–399 (2004).
85. E. O. Potma, D. J. Jones, J.-X. Cheng, X. S. Xie, and J. Ye, "High-sensitivity coherent anti-Stokes Raman scattering microscopy with two tightly synchronized picosecond lasers," Opt. Lett. **27**, 1168–1170 (2002).
86. F. Ganikhanov, S. Carrasco, X. S. Xie, M. Katz, W. Seitz, and D. Kopf, "Broadly tunable dual-wavelength light source for coherent anti-Stokes Raman scattering microscopy," Opt. Lett. **31**, 1292–1294 (2006).
87. N. Dudovich, D. Oron, and Y. Silberberg, "Single-pulse coherently controlled nonlinear Raman spectroscopy and microscopy," Nature **418**, 512–514 (2002).
88. T. W. Kee and M. T. Cicerone, "Simple approach to one-laser, broadband coherent anti-Stokes Raman scattering microscopy," Opt. Lett. **29**, 2701–2703 (2004).
89. S. H. Lim, A. G. Caster, and S. R. Leone, "Single pulse phase-control interferometric coherent anti-Stokes Raman scattering (CARS) spectroscopy," Phys. Rev. A **72**, 041803 (2005).
90. M. Jurna, J. P. Korterik, C. Otto, J. L. Herek, and H. L. Offerhaus, "Vibrational phase contrast microscopy by use of coherent anti-Stokes Raman scattering," Phys. Rev. Lett. **103**, 043905 (2009).
91. R. Hellwarth, J. Cherlow, and T. T. Yang, "Origin and frequency dependence of nonlinear optical susceptibilities of glasses," Phys. Rev. B **11**, 964–967 (1975).
92. D. McMorrow, W. T. Lotshaw, and G. A. Kenney-Wallace, "Femtosecond optical Kerr effect studies on the origin of nonlinear optical response in simple liquids," IEEE J. Quantum Electron. **24**, 443–454 (1988).
93. K. Isobe, T. Kawasumi, T. Tamaki, S. Kataoka, Y. Ozeki, and K. Itoh, "Three-dimensional profiling of refractive index distribution inside transparent materials by use of nonresonant four-wave-mixing microscopy," Appl. Phys. Express **1**, 022006 (2008).
94. D. Akimov, S. Chatzipapadopoulos, T. Meyer, N. Tarcea, B. Dietzek, M. Schmitt, and J. Popp, "Different contrast information obtained from CARS and nonresonant FWM images," J. Raman Spectrosc. **40**, 941–947 (2009).
95. B. C. Chen and S. H. Lim, "Three-dimensional imaging of director field orientations in liquid crystals by polarized four-wave-mixing microscopy," Appl. Phys. Lett. **94**, 171911 (2009).
96. A. G. Aronov, D. E. Pikus, and D. Shekter, "Quantum theory of free-electron dielectric constant in semiconductors," Sov. Phys. Solid State **10**,

645–647 (1968).
97. L. Bányai and S. W. Koch, "A simple theory for the effects of plasma screening on the optical spectra of highly excited semiconductors," Z. Phys. B **63**, 283–291 (1986).
98. H. Haug, ed., *Optical Nonlinearities and Instabilities in Semiconductors* (Academic, 1988).
99. H. Haug and S. W. Koch, *Quantum Theory of the Optical and Electronic Properties of Semiconductors* (World Scientific, 1990).
100. H. M. Gibbs, S. L. McCall, T. N. C. Vankatesan, A. C. Gossard, A. Passner, and W. Wiegmann, "Optical bistability in semiconductors," Appl. Phys. Lett. **35**, 451–453 (1979).
101. V. Kreminitskii, S. Odoulov, and M. Soskin, "Backward degenerate four-wave mixing in CdTe," Phys. Status Solidi A **57**, K71–K74 (1980).
102. R. K. Jain and D. G. Steel, "Large optical nonlinearities and cw degenerate four-wave mixing in HgCdTe," Opt. Commun. **43**, 72–77 (1982).
103. E. W. Van Stryland, M. W. Woodall, H. Vanherzeele, and M. J. Soileau, "Energy bandgap dependence of two-photon absorption," Opt. Lett. **10**, 490–492 (1985).
104. S. Schmitt-Rink, D. A. B. Miller, and D. S. Chemla, "Theory of the linear and nonlinear optical properties of semiconductor microcrystallites," Phys. Rev. B **35**, 8113–8125 (1987).
105. L. Brus, "Quantum crystallites and nonlinear optics," Appl. Phys. B **53**, 465–474 (1991).
106. L. I. Berger, "Properties of Semiconductors," in *CRC Handbook of Chemistry and Physics*, 90th ed., D. R. Lide, ed. (Taylor & Francis, 2009).
107. M. Sheik-Bahae, D. C. Hutchings, D. J. Hagan, and E. W. Van Stryland, "Dispersion of bound electronic nonlinear refraction in solids," IEEE J. Quantum Electron. **72**, 1296–1309 (1991).
108. S. Vijayalakshmi, M. A. George, and H. Grebel, "Nonlinear optical properties of silicon nanoclusters," Appl. Phys. Lett. **70**, 708–710 (1997).
109. G. Vijaya-Prakash, M. Cazzanelli, Z. Gaburro, L. Pavesi, F. Iacona, G. Franzó, and F. Priolo, "Nonlinear optical properties of silicon nanocrystals grown by plasma-enhanced chemical vapor deposition," J. Appl. Phys. **91**, 4607–4610 (2002).
110. Y. Cui, L. J. Lauhon, M. S. Gudiksen, J. Wang, and C. M. Lieber, "Diameter-controlled synthesis of single-crystal silicon nanowires," Appl. Phys. Lett. **78**, 2214–2216 (2001).
111. Y. Wu, Y. Cui, L. Huynh, C. J. Barrelet, D. C. Bell, and C. M. Lieber, "Controlled growth and structures of molecular-scale silicon nanowires," Nano Lett. **4**, 433–436 (2004).
112. A. G. Cullis, L. T. Canham, and P. D. J. Calcott, "The structural and luminescence properties of porous silicon," J. Appl. Phys. **82**, 909–965 (1997).
113. J. H. Park, L. Gu, G. V. Maltzahn, E. Ruoslahti, S. N. Bhatia, and M. J. Sailor, "Biodegradable luminescent porous silicon nanoparticles for *in vivo* applications," Nature Mater. **8**, 331–336 (2009).
114. R. Chen, D. L. Lin, and D. Mendoza, "Enhancement of the third-order nonlinear optical susceptibility in Si quantum wires," Phys. Rev. B **48**, 11879–11882 (1993).
115. Y. Jung, L. Tong, A. Tanaudommongkon, J. X. Cheng, and C. Yang, "*In vitro* and *in vivo* nonlinear optical imaging of silicon nanowires," Nano Lett. **9**, 2440–2444 (2009).
116. Y. Maeda, N. Tsukamoto, Y. Yazawa, Y. Kanemitsu, and M. Yasuaki, "Vis-

ible photoluminescence of Ge microcrystals embedded in $SiO_2$ glassy matrices," Appl. Phys. Lett. **59**, 3168–3170 (1991).
117. Q. Wan, C. L. Lin, N. L. Zhang, W. L. Liu, G. Yang, and T. H. Wang, "Linear and third-order nonlinear optical absorption of amorphous Ge nanoclusters embedded in $Al_2O_3$ matrix synthesized by electron-beam coevaporation," Appl. Phys. Lett. **82**, 3162–3164 (2003).
118. R. A. Ganeev, A. I. Ryasnyanskiy, and T. Usmanov, "Optical and nonlinear optical characteristics of the Ge and GaAs nanoparticle suspensions prepared by laser ablation," Opt. Commun. **272**, 242–246 (2006).
119. Y. Kanemitsu, H. Uto, Y. Masumoto, and Y. Maeda, "On the origin of visible photoluminescence in nanometer-size Ge crystallites," Appl. Phys. Lett. **61**, 2187–2189 (1992).
120. L. Balan, R. Schneider, D. Billaud, and J. Ghanbaja, "A new organicmetallic synthesis of size-controlled tin(0) nanoparticles," Nanotechnology **16**, 1153–1158 (2005).
121. D. H. Webber and R. L. Brutchey, "Photolytic preparation of tellurium nanorods," Chem. Commun. (Cambridge), 5701–5703 (2009).
122. S.-H. Kim and T. Yoko, ″Nonlinear optical properties of $TiO_2$-based glasses: $MO_x$–$TiO_2$ (M = Sc, Ti, V, Nb, Mo, Ta and W) binary glasses,″ J. Am. Ceram. Soc. **78**, 1061–1065 (1995).
123. W. E. Torruellas, L. A. Weller-Brophy, R. Zanoni, G. I. Stegeman, Z. Osborne, and B. J. J. Zelinski, "Third-harmonic generation measurement of nonlinearities in $SiO_2$-$TiO_2$ sol-gel films," Appl. Phys. Lett. **58**, 1128–1130 (1991).
124. T. Hashimoto, T. Yamada, and T. Yoko, "Third order nonlinear optical properties of sol-gel derived $\alpha$-$Fe_2O_3$, $\gamma$-$Fe_2O_3$, and $Fe_3O_4$ thin films.," J. Appl. Phys. **80**, 3184–3190 (1996).
125. R. Desalvo, A. A. Said, D. J. Hagan, and E. W. Van Stryland, "Infrared to ultraviolet measurements of two-photon absorption and $n_2$ in wide bandgap solids," IEEE J. Quantum Electron. **32**, 1324–1333 (1996).
126. T. Hashimoto, T. Yoko, and S. Sakka, "Third-order nonlinear optical susceptibility of $\alpha$-$Fe_2O_3$ thin film prepared by the sol-gel method," J. Ceram. Soc. Jpn. **101**, 64–68 (1993).
127. T. Hashimoto, T. Yoko, and S. Sakka, "Sol-gel preparation and third-order nonlinear optical properties of $TiO_2$ thin films," Bull. Chem. Soc. Jpn. **67**, 653–660 (1994).
128. L. J. Li, K. Yu, and Y. Wang, "Synthesis and field emission of $SnO_2$ nanowalls," Cryst. Res. Technol. **44**, 1245–1248 (2009).
129. N. Ueda, H. Kawazoe, Y. Watanabe, M. Takata, M. Yamane, and K. Kubodera, "Third-order nonlinear optical susceptibilities of electroconductive oxide thin films," Appl. Phys. Lett. **59**, 502–503 (1991).
130. A. Walsh, J. L. F. DaSilva, S. Wei, C. Korber, A. Klein, L. F. J. Piper, A. DeMasi, K. E. Smith, G. Panaccione, P. Torelli, D. J. Payne, A. Bourlange, and R. E. Egdell, "Nature of the band gap of $In_2O_3$ revealed by first-principles calculations and x-ray spectroscopy," Phys. Rev. Lett. **100**, 167402 (2008).
131. S. Kim, T. Yoko, and S. Sakka, "Linear and nonlinear optical properties of $TeO_2$ glass," J. Am. Ceram. Soc. **76**, 2486–2490 (1993).
132. M. Larciprete, D. Heartle, A. Berladini, M. Bertolotto, F. Sarto, and P. Günter, "Characterization of second and third-order optical nonlinearities of ZnO sputtered films," Appl. Phys. B **82**, 431–437 (2006).
133. T. Hashimoto and T. Yoko, "Third-order nonlinear optical properties of

sol-gel derived $V_2O_5$, $Nb_2O_5$ and $Ta_2O_3$ thin films," Appl. Opt. **34**, 2941–2948 (1995).
134. J.-H. Lin, Y.-J. Chen, H.-Y. Lin, and W.-F. Hsieh, "Two-photon resonance assisted huge nonlinear refraction and absorption in ZnO thin films," J. Appl. Phys. **97**, 033526 (2005).
135. S. P. Kowalczyk, F. R. McFeely, L. Ley, V. T. Gritsyna, and D. A. Shirley, "The electronic structure of $SrTiO_3$ and some simple related oxides (MgO, $Al_2O_3$, SrO, $TiO_2$)," Solid State Commun. **23**, 161–169 (1977).
136. S. Tsunekawa, J. T. Wang, Y. Kawazoe, and A. Kasuya, "Blueshifts in the ultraviolet absorption spectra of cerium oxide nanocrystallites," J. Appl. Phys. **94**, 3654–3656 (2003).
137. J. C. Johnson, H. Yan, R. D. Schaller, P. B. Petersen, P. Yang, and R. J. Saykally, "Near-field imaging of nonlinear optical mixing in single zinc oxide nanowires," Nano Lett. **2**, 279–283 (2002).
138. H. Chen, H. Wang, M. N. Slipchenko, Y. Jung, Y. Shi, J. Zhu, K. K. Buhman, and J. X. Cheng, "A multimodal platform for nonlinear optical microscopy and microspectroscopy," Opt. Express **17**, 1282–1290 (2009).
139. J. Moger, B. D. Johnston, and C. R. Tyler, "Imaging metal oxide nanoparticles in biological structures with CARS microscopy," Opt. Express **16**, 3408–3419 (2008).
140. B. Yu, C. Zhu, and F. Gan, "Large nonlinear optical properties of $Fe_2O_3$ nanoparticles," Physica E (Amsterdam) **8**, 360–364 (2000).
141. K. C. Rustagi and C. Flytzanis, "Optical nonlinearities in semiconductor-doped glasses," Opt. Lett. **9**, 344–346 (1984).
142. D. Ricard, P. Roussignol, F. Hache, and C. Flytzanis, "Nonlinear optical properties of quantum confined semiconductor microcrystallites," Phys. Status Solidi B **159**, 275–284 (1990).
143. I. Gerdova and A. Haché, "Third-order nonlinear spectroscopy of CdSe and CdSe/ZnS core shell quantum dots," Opt. Commun. **246**, 205–212 (2004).
144. G. P. Banfi, V. Degiorgio, and D. Ricard, "Nonlinear optical properties of semiconductor nanocrystals," Adv. Phys. **47**, 447–510 (1998).
145. J. Shah, *Ultrafast Processes in Semiconductors and Semiconductor Nanostructures* (Springer, 1996).
146. N. H. Bonadeo, G. Chen, D. Gammon, D. S. Katzer, D. Park, and D. G. Steel, "Nonlinear nano-optics: probing one exciton at the time," Phys. Rev. Lett. **81**, 2759–2762 (1998).
147. T. Guenther, C. Lienau, T. Elsaesser, M. Glanemann, V. M. Axt, T. Kuhn, S. Eshlaghi, and A. D. Wieck, "Coherent nonlinear optical response of single quantum dots studied by ultrafast near-field spectroscopy," Phys. Rev. Lett. **89**, 057401 (2002).
148. G. Chen, N. H. Bonadeo, D. G. Steel, D. Gammon, D. S. Katzer, D. Park, and L. J. Sham, "Optically induced entanglement of excitons in a single quantum dot," Science **289**, 1906–1909 (2000).
149. S. Adachi, *Properties of Group IV, III–V and II–VI Semiconductors* (Wiley, 2005).
150. W. C. W. Chan, D. J. Maxwell, X. Gao, R. E. Bailey, M. Han, and S. Nie, "Luminscent quantum dots for multiplexed biological detection and imaging," Curr. Opin. Biotechnol. **13**, 40–46 (2002).
151. A. P. Alivisatos, W. Gu, and C. Larabell, "Quantum dots as cellular probes," Annu. Rev. Biomed. Eng. **7**, 55–76 (2005).
152. A. V. Fedorov, A. V. Baranov, and K. Inoue, "Two-photon transitions in

systems with semiconductor quantum dots," Phys. Rev. B **54**, 8627–8632 (1996).
153. L. A. Padilha, J. Hu, D. J. Hagan, E. W. Van Stryland, C. L. Cesar, L. Barboza, and C. H. B. Cruz, "Two-photon absorption in CdTe quantum dots," Opt. Express **13**, 6460–6467 (2005).
154. L. A. Padhilla, J. Fu, D. J. Hagan, E. W. Van Stryland, C. L. Cesar, L. C. Barbosa, C. H. B. Cruz, D. Buso, and A. Martucci, "Frequency degenerate and nondegenerate two-photon absorption spectra of semiconductor quantum dots," Phys. Rev. B **75**, 075325 (2007).
155. S. C. Kung, W. E. v. d. Veer, F. Yang, K. C. Donavan, and R. M. Penner, "20 $\mu$s photocurrent response from lithographically patterned nanocrystalline cadmium selenide nanowires," Nano Lett. 10, 1481–1485 (2010).
156. D. D. Smith, Y. Yoon, R. W. Boyd, J. K. Campbell, L. A. Baker, R. M. Crooks, and M. George, "Z-scan measurement of the nonlinear absorption of a thin gold film," J. Appl. Phys. **86**, 6200–6205 (1999).
157. D. Ricard, P. Roussignol, and C. Flytzanis, "Surface mediated enhancement of optical phase conjugation in metal colloids," Opt. Lett. **10**, 511–513 (1985).
158. M. L. Brongersma and P. G. Kik, eds., *Surface Plasmon Nanophotonics* (Springer, 2007).
159. V. M. Agranovich and D. L. Mills, eds., *Surface Polaritons—Electromagnetic Waves at Surfaces and Interfaces* (North-Holland, 1982).
160. A. Otto, "Excitation of nonradiative surface plasma waves in silver by the method of frustrated total reflection," Z. Phys. A: Hadrons Nucl. **241**, 820–822 (1968).
161. E. Kretschmann and H. Raether, "Radiative decay of non radiative plasmons excited by light," Z. Naturforsch. A **23**, 2135–2136 (1968).
162. F. López-Tejeira, S. G. Rodrigo, L. Martín-Moreno, F. J. García-Vidal, E. Devaux, T. W. Ebbesen, J. R. Krenn, I. P. Radko, S. I. Bozhevolnyi, M. U. González, J. C. Weeber, and A. Dereux, "Efficient unidirectional nanoslit couplers for surface plasmons," Nat. Phys. **3**, 324–328 (2007).
163. A. Bouhelier, F. Ignatovich, A. Bruyant, C. Huang, G. C. d. Francs, J.-C. Weeber, A. Dereux, G. P. Wiederrecht, and L. Novotny, "Surface plasmon interference excited by tightly focused laser beams," Opt. Lett. **32**, 2535–2537 (2007).
164. H. J. Simon, D. E. Mitchell, and J. G. Watson, "Optical second-harmonic generation with surface plasmons in silver films," Phys. Rev. Lett. **33**, 1531–1534 (1974).
165. H. J. Simon, R. E. Benner, and J. G. Rako, "Optical second harmonic generation with surface plasmons in piezoelectric crystals," Opt. Commun. **23**, 245–248 (1977).
166. S. Palomba and L. Novotny, "Nonlinear excitation of surface plasmon polaritons by four-wave-mixing," Phys. Rev. Lett. **101**, 056802 (2008).
167. F. De Martini and Y. R. Shen, "Nonlinear excitations of surface polaritons," Phys. Rev. Lett. **36**, 216–219 (1976).
168. F. De Martini, G. Giuliani, P. Mataloni, E. Palange, and Y. R. Shen, "Study of surface polaritons in GaP by optical four-wave-mixing," Phys. Rev. Lett. **37**, 440–443 (1976).
169. C. K. Chen, A. R. B. de Castro, and Y. R. Shen, "Surface coherent anti-Stokes Raman spectroscopy," Phys. Rev. Lett. **43**, 946–949 (1979).
170. T. Y. F. Tsang, "Surface-plasmon-enhanced third-harmonic generation in thin silver films," Opt. Lett. **21**, 245–247 (1996).

171. J. Renger, R. Quidant, N. v. Hulst, S. Palomba, and L. Novotny, "Free-space excitation of propagating surface plasmon polaritons by nonlinear four-wave-mixing," Phys. Rev. Lett. **103**, 266802 (2009).
172. J. Renger, R. Quidant, N. v. Hulst, and L. Novotny, "Surface-enhanced nonlinear four-wave-mixing," Phys. Rev. Lett. **104**, 046803 (2010).
173. G. Mie, "A contribution to the optics of turbid media, particularly of coloidal metallic suspensions," Ann. Phys. **25**, 377–452 (1908).
174. K. Lance-Kelly, E. Coronado, L. L. Zhao, and G. C. Schatz, "The optical properties of metal nanoparticles: the influence of size, shape, and dielectric environment," J. Phys. Chem. B **107**, 668–677 (2003).
175. P. K. Jain, K. S. Lee, I. H. El-Sayed, and M. A. El-Sayed, "Calculated absorption and scattering properties of gold nanoparticles of different size, shape, and composition: applications in biological imaging and biomedicine," J. Phys. Chem. B **110**, 7238–7248 (2006).
176. A. Jara, R. E. Arias, and D. L. Mills, "Plasmon and the electromagnetic respons of nanowires," Phys. Rev. B **81**, 085422 (2010).
177. A. Taflove and S. C. Hagness, *Computational Electrodynamics: the Finite Difference Time-Domain Method* (Artech House, 2000).
178. J. C. Maxwell-Garnett, "Colours in metal glasses and in metal films," Philos. Trans. R. Soc. London **203**, 385 (1904).
179. D. S. Chemla, J. P. Heritage, P. F. Liao, and E. D. Isaacs, "Enhanced four-wave mixing from silver particles," Phys. Rev. B **27**, 4553–4558 (1983).
180. L. Genzel, T. P. Martin, and U. Kreibig, "Dielectric function and plasma resonances of small metal particles," Z. Phys. B **21**, 339–346 (1975).
181. U. Kreibig and C. V. Fragstein, "The limitation of mean free path in small silver particles," Z. Phys. **224**, 307–323 (1969).
182. F. Hache, D. Ricard, C. Flytzanis, and U. Kreibig, "The optical Kerr effect in small metal particles and metal colloids: the case of gold," Appl. Phys. A **47**, 347–357 (1988).
183. M. J. Bloemer, J. W. Haus, and P. R. Ashley, "Degenerate four-wave-mixing in colloidal gold as a function of particle size," J. Opt. Soc. Am. B **7**, 790–795 (1990).
184. K. Uchida, S. Kaneko, S. Omi, C. Hata, H. Tanji, Y. Asahara, A. J. Ikushima, T. Tokizaki, and A. Nakamura, "Optical nonlinearities of a high concentration of small metal particles dispersed in glass: copper and silver particles," J. Opt. Soc. Am. B **11**, 1236–1243 (1994).
185. S. Palomba, M. Danckwerts, and L. Novotny, "Nonlinear plasmonics with gold nanoparticle antennas," J. Opt. A, Pure Appl. Opt. **11**, 114030 (2009).
186. G. T. Boyd, Z. H. Yu, and Y. R. Shen, "Photoinduced luminescence from the noble metals and its enhancement on roughened surfaces," Phys. Rev. B **33**, 7923–7936 (1986).
187. D. Yelin, D. Oron, S. Thiberge, E. Moses, and Y. Silberberg, "Multiphoton plasmon-resonance microscopy," Opt. Express **11**, 1385–1391 (2003).
188. R. A. Farrer, F. L. Butterfield, V. W. Chen, and J. T. Fourkas, "Highly efficient multiphoton-absorption-induced luminescence from gold nanoparticles," Nano Lett. **5**, 1139–1142 (2005).
189. H. Wang, T. B. Huff, D. A. Zweifel, W. He, P. S. Low, A. Wei, and J.-X. Cheng, "*In vitro* and *in vivo* two-photon luminescence imaging of single gold nanorods," Proc. Natl. Acad. Sci. U.S.A. **102**, 15752–15756 (2005).
190. G. T. Boyd, T. Rasing, J. R. R. Leite, and Y. R. Shen, "Local-field enhancement on rough surfaces of metals, semimetals, and semiconductors with the use of optical second-harmonic generation," Phys. Rev. B **30**, 519–525

(1984).
191. J. Gersten and A. Nitzan, "Electromagnetic theory of enhanced Raman scattering by molecules adsorbed on rough surfaces," J. Chem. Phys. **73**, 3023–3037 (1980).
192. P. F. Liao and A. Wokaun, "Lightning rod effect in surface enhanced Raman scattering," J. Chem. Phys. **76**, 751–752 (1982).
193. K. Kneipp, R. R. Dasari, and Y. Wang, "Near-infrared surface-enhances Raman scattering (NIR SERS) on colloidal silver and gold," Appl. Spectrosc. **48**, 951–955 (1994).
194. P. C. Lee and D. Meisel, "Absorption and surface-enhanced Raman of dyes on silver an gold sols," J. Phys. Chem. **86**, 3391–3395 (1982).
195. M. Moskovits, "Surface-enhanced spectroscopy," Rev. Mod. Phys. **57**, 783–826 (1985).
196. S. Nie and S. R. Emory, "Probing single molecules and single nanoparticles by surface-enhanced Raman scattering," Science **275**, 1102–1106 (1997).
197. A. Otto, I. Mrozek, H. Grabborn, and A. Akermann, "Surface-enhanced Raman scattering," J. Phys. Condens. Matter **4**, 1143–1212 (1992).
198. J. X. Cheng, L. D. Book, and X. S. Xie, "Polarization coherent anti-Stokes Raman scattering microscopy," Opt. Lett. **26**, 1341–1343 (2001).
199. J. L. Oudar, R. W. Smith, and Y. R. Shen, "Polarization-sensitive coherent anti-Stokes Raman spectroscopy," Appl. Phys. Lett. **34**, 758–760 (1979).
200. A. Volkmer, L. D. Book, and X. S. Xie, "Time-resolved coherent anti-Stokes Raman scattering microscopy: imaging based on Raman free induction decay," Appl. Phys. Lett. **80**, 1505–1507 (2002).
201. M. Jurna, J. P. Korterik, C. Otto, and H. L. Offerhaus, "Shot noise limited heterodyne detection of CARS signals," Opt. Express **15**, 15207–15213 (2007).
202. E. O. Potma, C. L. Evans, and X. S. Xie, "Heterodyne coherent anti-Stokes Raman scattering (CARS) imaging," Opt. Lett. **31**, 241–243 (2006).
203. S. Link, C. Burda, M. B. Mohamed, B. Nikoobakht, and M. A. El-Sayed, "Laser photothermal melting and fragmentation of gold nanorods: energy and laser pulse-width dependence," J. Phys. Chem. A **103**, 1165–1170 (1999).
204. S. Link, C. Burda, B. Nikoobakht, and M. A. El-Sayed, "Laser-induced shape changes of colloidal gold nanorods using femtosecond and nanosecond laser pulses," J. Phys. Chem. B **104**, 6152–6163 (2000).
205. A. Bouhelier, R. Bachelot, G. Lerondel, S. Kostcheev, P. Royer, and G. P. Wiederrecht, "Surface plasmon characteristics of tunable photoluminescence in single gold nanorods," Phys. Rev. Lett. **95**, 267405 (2005).
206. T. W. Koo, S. Chan, and A. A. Berlin, "Single-molecule detection of biomolecules by surface-enhanced coherent anti-Stokes Raman scattering," Opt. Lett. **30**, 1024–1026 (2005).
207. T. Ichimura, N. Hayazawa, M. Hashimoto, Y. Inouye, and S. Kawata, "Local enhancement of coherent anti-Stokes Raman scattering by isolated gold nanoparticles," J. Raman Spectrosc. **34**, 651–654 (2003).
208. T. Ichimura, N. Hayazawa, M. Hashimoto, Y. Inouye, and S. Kawata, "Tip-enhanced coherent anti-Stokes Raman scattering for vibrational nanoimaging," Phys. Rev. Lett. **92**, 220801 (2004).
209. H. S. Nalwa and S. Miyata, *Nonlinear Optics of Organic Molecules and Polymers* (CRC Press, 1997).
210. H. Nakanishi and H. Katagi, "Microcrystals of polydiacetylene derivatives

and their linear and nonlinear optical properties," Supramol. Sci. **5**, 289–295 (1998).
211. H. B. Fu and J. N. Yao, "Size effects on the optical properties of organic nanoparticles," J. Am. Chem. Soc. **123**, 1434–1439 (2001).
212. H. Masuhara, H. Nakanishi, and K. Sasaki, eds., *Single Organic Nanoparticles* (Springer-Verlag, 2003).
213. S. M. Nie and R. N. Zare, "Optical detection of single molecules," Annu. Rev. Biophys. Biomol. Struct. **26**, 567–596 (1997).
214. T. Plakhotnik, E. A. Donley, and U. P. Wild, "Single-molecule spectroscopy," Annu. Rev. Phys. Chem. **48**, 181–212 (1997).
215. W. E. Moerner, "High-resolution optical spectroscopy of single molecules in solids," Acc. Chem. Res. **29**, 563–571 (1996).
216. X. S. Xie, "Single molecule approach to enzymology," Single Mol. **2**, 229–236 (2001).
217. X. S. Xie, "Single-molecule approach to dispersed kinetics and dynamic disorder: probing conformational fluctuation and enzymatic dynamics," J. Chem. Phys. **117**, 11024–11032 (2002).
218. S. Weiss, "Measuring conformational dynamics of biomolecules by single molecule fluorescence spectroscopy," Nat. Struct. Biol. **7**, 724–729 (2000).
219. E. M. H. P. van Dijk, J. Hernando, J. J. García-López, M. Crego-Calama, D. N. Reinhoudt, L. Kuipers, M. F. García-Parajó, and N. F. van Hulst, "Single-molecule pump–probe detection resolves ultrafast pathways in individual quantum coupled systems," Phys. Rev. Lett. **94**, 078302 (2005).
220. W. Min, S. Lu, M. Rueckel, G. R. Holtom, and X. S. Xie, "Near-degenerate four-wave-mixing microscopy," Nano Lett. **9**, 2423–2426 (2009).
221. R. Saito, G. Dresselhaus, and M. S. Dresselhaus, *Physical Properties of Carbon Nanotubes* (Imperial, 1998).
222. J. S. Lauret, C. Voisin, G. Cassabois, J. Tignon, C. Delalande, P. Roussignol, O. Jost, and L. Capes, "Third-order optical nonlinearities of carbon nanotubes in the femtosecond regime," Appl. Phys. Lett. **85**, 3572–3574 (2004).
223. S. Botti, R. Ciardi, L. De Dominicis, L. S. Asilyan, R. Fantoni, and T. Marolo, "DFWM measurements of third-order susceptibility of single-wall carbon nanotubes grown without catalyst," Chem. Phys. Lett. **378**, 117–121 (2003).
224. X. Liu, J. Si, B. Chang, G. Xu, Q. Yang, Z. Pan, S. Xie, P. Ye, J. Fan, and M. Wan, "Third-order optical nonlinearity of the carbon nanotubes," Appl. Phys. Lett. **74**, 164–166 (1999).
225. H. Kim, T. Sheps, P. G. Collins, and E. O. Potma, "Nonlinear optical imaging of individual carbon nanotubes with four-wave-mixing microscopy," Nano Lett. **9**, 2991–2995 (2009).
226. J. S. Lauret, C. Voisin, G. Cassabois, C. Delalande, P. Roussignol, O. Jost, and L. Capes, "Ultrafast carrier dynamics in single-wall carbon nanotubes," Phys. Rev. Lett. **90**, 057404 (2003).
227. C. Manzoni, A. Gambetta, E. Menna, M. Meneghetti, G. Lanzani, and G. Cerullo, "Intersubband exciton relaxation dynamics in single-walled carbon nanotubes," Phys. Rev. Lett. **94**, 207401 (2005).
228. H. Y. Seferyan, M. B. Nasr, V. Senekerimyam, R. Zadoyan, P. Collins, and V. A. Apkarian, "Transient grating measurements of excitonic dynamics in single walled carbon nanotubes: the dark excitonic bottleneck," Nano Lett. **6**, 1757–1760 (2006).

229. L. Huang, H. N. Pedrosa, and T. D. Krauss, "Ultrafast ground-state recovery of single-walled carbon nanotubes," Phys. Rev. Lett. **93**, 017403 (2004).
230. C. A. Marx, U. Harbola, and S. Mukamel, "Nonlinear optical spectroscopy of single, few and many molecules: nonequilibrium Green's function QED approach," Phys. Rev. A **77**, 022110 (2008).
231. O. Roslyak, C. Marx, and S. Mukamel, "Generalized Kramers–Heisenberg expressions for stimulated Raman scattering and two-photon absorption," Phys. Rev. A **79**, 063827 (2009).
232. R. Ranav and S. Mukamel, "Stimulated coherent anti-Stokes Raman spectroscopy (CARS) resonances originate from double-slit interference of two-photon Stokes pathways," Proc. Natl. Acad. Sci. U.S.A. **107**, 4825–4829 (2010).

**Yong Wang** received his B.S. degree from the University of Science and Technology of China, China, in 2007. He is currently working toward obtaining his Ph.D. in the Chemistry Department of the University of California, Irvine, in the laboratory of Prof. Eric O. Potma. His current research includes studying both linear and nonlinear plasmonic properties of metal films in the femtosecond regime and electronic properties of single molecules through surface plasmon polaritons.

**Chia-Yu Lin** obtained her B.S. degree in 2005 from National Taiwan University, Taipei, Taiwan. Since receiving her M.S. degree in 2006 from the University of California, Irvine, she has been working as a Ph.D. student under the supervision of Prof. Eric O. Potma. She is interested in applying nonlinear optical techniques for the purpose of visualizing biological samples and characterizing nanostructures.

**Alexei Nikolaenko** obtained his M.S. degree in Applied Physics and Mathematics from Moscow Institute of Physics and Technology, State University (M.I.P.T.) in 2002. Later that year, he joined Prof. Guenter Ahlers' laboratory at the University of California, Santa Barbara, where he worked three years as a Post-graduate Researcher in the Department of Physics. Since 2005, he is a Ph.D. candidate at the University of California, Irvine. His current research interests include the development of new imaging techniques based on nonlinear optical phenomena.

**Varun Raghunathan** completed his Ph.D. in 2008 from University of California, Los Angeles. He is currently working as a postdoctoral researcher in the chemistry department at University of California, Irvine, where he is working on developing novel nonlinear imaging techniques. His research interests are in the areas of applied nonlinear optics, semiconductors, optoelectronics and quantum electronics.

**Eric O. Potma** obtained his Ph.D. in 2001 from the University of Groningen, the Netherlands. He spent four years as a postdoctoral fellow in the group of Professor X. Sunney Xie at Harvard University in Cambridge, Massachusetts. In 2005, he joined the Chemistry Department of the University of California, Irvine, as an Assistant Professor. His research group is active in developing nonlinear optical imaging techniques for the purpose of interrogating biological tissues and nanostructured materials.